© 2020. Published by The Company of Biologists Ltd | Development (2020) 147, dev187526. doi:10.1242/dev.187526

RESEARCH ARTICLE

Transcriptional regulation of MGE progenitor proliferation by PRDM16 controls cortical GABAergic interneuron production

Miguel Turrero García[1], José-Manuel Baizabal[1,*], Diana N. Tran[1], Rui Peixoto[2,‡], Wengang Wang[2], Yajun Xie[1], Manal A. Adam[1], Lauren A. English[3,§], Christopher M. Reid[1], Salvador I. Brito[1,¶], Matthew A. Booker[4], Michael Y. Tolstorukov[3] and Corey C. Harwell[1,]**

ABSTRACT

The mammalian cortex is populated by neurons derived from neural progenitors located throughout the embryonic telencephalon. Excitatory neurons are derived from the dorsal telencephalon, whereas inhibitory interneurons are generated in its ventral portion. The transcriptional regulator PRDM16 is expressed by radial glia, neural progenitors present in both regions; however, its mechanisms of action are still not fully understood. It is unclear whether PRDM16 plays a similar role in neurogenesis in both dorsal and ventral progenitor lineages and, if so, whether it regulates common or unique networks of genes. Here, we show that *Prdm16* expression in mouse medial ganglionic eminence (MGE) progenitors is required for maintaining their proliferative capacity and for the production of proper numbers of forebrain GABAergic interneurons. PRDM16 binds to cis-regulatory elements and represses the expression of region-specific neuronal differentiation genes, thereby controlling the timing of neuronal maturation. PRDM16 regulates convergent developmental gene expression programs in the cortex and MGE, which utilize both common and region-specific sets of genes to control the proliferative capacity of neural progenitors, ensuring the generation of correct numbers of cortical neurons.

KEY WORDS: CNS development, Neural progenitors, Medial ganglionic eminence, Cortical interneurons, *Prdm16*

INTRODUCTION

The complex circuitry of the mammalian neocortex comprises two major types of neuronal cells, excitatory pyramidal neurons and inhibitory interneurons, with different functions and origins (Campbell, 2003; Wilson and Rubenstein, 2000). In the mouse, both types of neurons are generated between embryonic day (E)10 and E16, from neural progenitors residing in the proliferative zones located along the lateral ventricles of the telencephalon (Anthony et al., 2004; Marin and Muller, 2014). Excitatory neurons are produced from dorsal (pallial) telencephalic proliferative zones (Govindan and Jabaudon, 2017), whereas the majority of inhibitory interneurons are produced from two transient proliferative structures in the ventral (subpallial) telencephalon, known as the medial (MGE) and caudal (CGE) ganglionic eminences (Miyoshi et al., 2010; Nery et al., 2002; Wonders and Anderson, 2006; Xu et al., 2004). Progenitors in the MGE give rise to two major groups of inhibitory interneurons, fast-spiking and non-fast-spiking, which can be identified by their expression of the markers parvalbumin (PV) and somatostatin (SST), respectively (Xu et al., 2004). The majority of SST-expressing interneurons are born in the early stages of neurogenesis, whereas PV-expressing cells are generated later (Hu et al., 2017; Miyoshi et al., 2007). Both populations undergo a process of tangential migration into the developing cortex, following a spatiotemporal pattern in which earlier born cells typically occupy the deep layers of the cortex, whereas later born cells occupy more superficial layers (Lopez-Bendito et al., 2004). During neurogenesis, neural progenitors in the MGE transition through a series of competence states as they produce these two types of interneurons: radial glia (RG) divide at the surface of the ventricle, self-renewing while giving rise to either neurons (direct neurogenesis) or more committed transit-amplifying progenitors with limited self-renewal capacity, that usually divide once to generate two neurons (indirect neurogenesis) (Harwell et al., 2015; Turrero Garcia and Harwell, 2017). In order to understand how the balance of excitation and inhibition is achieved during development and maintained in the mature cortex, it is necessary to know the mechanisms by which MGE progenitors regulate their proliferation and consequently their neuronal output (Lim et al., 2018; Petryniak et al., 2007). One crucial factor that ensures correct neural progenitor amplification and cell lineage progression is PRDM16, a transcriptional regulator that is specifically expressed in radial glia of the developing telencephalon (Baizabal et al., 2018; Chuikov et al., 2010; Shimada et al., 2017). In the cortex, *Prdm16* controls indirect neurogenic divisions, radial glia lineage progression and the production of late born upper layer pyramidal neurons by regulating the epigenetic state of developmental enhancers (Baizabal et al., 2018). *Prdm16* is also expressed in radial glia of the MGE, but it is unknown whether it regulates lineage progression programs controlling the production of cortical interneurons. Here we show that *Prdm16* expression in MGE progenitors is necessary in order to maintain their proliferative potential and ensure the generation of sufficient numbers of cortical interneurons and the maintenance of correct inhibitory input onto pyramidal cells. PRDM16 controls the expression of both generic and MGE-specific neuronal differentiation programs through its binding to sets of cis-regulatory elements that are either common between this area and the developing neocortex or exclusive to the MGE.

RESULTS

Prdm16 expression in MGE progenitors regulates the number of cortical interneurons

We generated a Cre-lox system-based conditional knockout mouse model, in which *Prdm16* was deleted in cells with a developmental

[1]Department of Neurobiology, Harvard Medical School, Boston, MA 02115, USA. [2]Howard Hughes Medical Institute, Department of Neurobiology, Harvard Medical School, Boston, MA 02115, USA. [3]Summer Honors Undergraduate Research Program, Harvard Medical School, Boston, MA 02115, USA. [4]Department of Informatics and Analytics, Dana-Farber Cancer Institute, Boston, MA 02115, USA. *Present address: Department of Biology, Indiana University, Bloomington, IN 47405, USA. ‡Present address: Department of Psychiatry, University of Pittsburgh, Pittsburgh, PA 15219, USA. §Present address: Neuroscience Training Program, University of Wisconsin-Madison, Madison, WI 53705, USA. ¶Present address: Department of Neurobiology, Boston Children's Hospital, Boston, MA 02115, USA.

**Author for correspondence (corey_harwell@hms.harvard.edu)

C.C.H., 0000-0002-8043-5869

Handling Editor: François Guillemot
Received 17 December 2019; Accepted 5 October 2020

Development (2020) 147, dev187526. doi:10.1242/dev.187526

history of *Nkx2.1* expression (i.e. neural progenitors in the MGE and their progeny) (Cohen et al., 2014; Xu et al., 2008). Additionally, these mice carried a Cre-dependent fluorescent reporter, tdTomato (tdT), to allow identification of cortical interneurons derived from *Nkx2.1*-expressing MGE progenitors in the adult brain after the expression of this gene is shut down (Fig. 1A,C) (Madisen et al., 2010). To verify the specific ablation of *Prdm16* in *Nkx2.1*-expressing cells, we examined the brains of wild-type (WT) and conditional knockout (cKO) mice at E13, a developmental stage midway through cortical interneuron neurogenesis (Turrero Garcia and Harwell, 2017), confirming the absence of PRDM16 in the ventricular zone of the MGE by immunostaining (Fig. 1B). We analyzed the brains of postnatal day (P)30 mice in order to understand the consequences of *Prdm16* deletion in the mature cortex. We performed immunofluorescence staining to detect tdT, SST and PV, markers of the two major subgroups of MGE-derived forebrain interneurons (Fig. 1C). We found that the number of tdT-positive (tdT^+) interneurons in cKO cortices was 27.27% lower than in WT controls (Fig. 1D). Decreased numbers of tdT^+ cells were observed across all cortical layers except for layer VI (Fig. 1E), and the proportion of tdT^+ cells that were positive for either SST or PV was the same in WT (27.39% SST^+ and 29.96% PV^+) and cKO cortices (26.60% SST^+ and 27.30% PV^+). The total numbers of tdT^+ cortical interneurons expressing SST (Fig. 1F) or PV (Fig. 1H) were decreased by similar proportions as the overall tdT^+ cells (30.43% in SST^+ and 35.03% in PV^+ cells). The loss of SST^+ (Fig. 1G) and PV^+ (Fig. 1I) in tdT^+ cortical interneurons was also observed across all cortical layers except for layer VI. We observed a similar phenotype in the hippocampus (Fig. S1A), where there was a decrease in the number of tdT^+ *Nkx2.1*-lineage interneurons (Fig. S1B), which was consistent across all regions except the subiculum (Fig. S1C), and across all layers (Fig. S1D). In the hippocampus, the loss was cell type-specific: the number of SST^+, tdT^+ cells was decreased (Fig. S1E), whereas, unexpectedly, PV^+, tdT^+ cells were not affected (Fig. S1F). As in the cortex, the distribution of tdT^+ cells in the hippocampus of cKO mice closely recapitulated that of the WT in all areas (Fig. S1G,H). There was a trend toward decreased numbers of *Nkx2.1*-lineage cells in the striatum of cKO animals (Fig. S1I) and a significant reduction in the nucleus accumbens (Fig. S1J). Together, these observations indicate that *Prdm16* regulates the number of *Nkx2.1*-lineage cells throughout the forebrain; this effect was particularly clear for MGE-derived interneurons in the adult cortex and hippocampus.

Partial compensation for loss of MGE-derived cortical interneurons in the cKO cortex

The proper complement of inhibitory interneurons is essential for maintaining the excitatory and inhibitory network balance; however, cKO mice do not display obvious seizure activity despite the decrease in PV^+ and SST^+ cortical interneurons (Neves et al., 2013; Southwell et al., 2014). We hypothesized that a decrease in inhibitory tone due to the loss of MGE-derived interneurons in the cKO cortex could be compensated by populations derived from another major embryonic source of cortical inhibitory neurons, the caudal ganglionic eminence (CGE) (Denaxa et al., 2018). To test this, we performed immunofluorescence staining in P30 WT and cKO brains to detect reelin and vasointestinal peptide (VIP), two markers of CGE-derived cortical interneurons (Fig. 2A) (Lee et al., 2010; Miyoshi et al., 2010). We did not detect a significant difference in the total number of VIP^+ (Fig. 2B) or $reelin^+$ (Fig. 2C) cortical interneurons. Their distribution across cortical layers I-VI was largely similar between WT and cKO animals (Fig. S2A,B); however, there was a significant increase in the number of $reelin^+$ cells in layer I of the mutant cortex (Fig. S2B). $Reelin^+$ interneurons originate from either the CGE or the MGE (Miyoshi et al., 2010); the latter population is largely SST^+ (Pesold et al., 1999). To distinguish between these two $reelin^+$ subpopulations, we quantified the proportion of cortical $reelin^+$ cells that were tdT^+, as cells labeled with the Nkx2.1-Cre driver line originate in the MGE. We found that approximately two-thirds (67.16%) of $reelin^+$ interneurons in WT cortices were MGE-derived, but this proportion was significantly lower (52.41%) in cKO mice (Fig. 2D). In line with this, cKO cortices contained an increased number of CGE-derived (i.e. tdT^-) $reelin^+$ interneurons (Fig. 2E), concentrated in cortical layers I and II-III (Fig. 2F). We did not observe an analogous increase in the VIP^+ population (Fig. S2A). These results suggest that there is an increase in the number of CGE-derived interneurons in the upper layers of cKO cortices, which could partially compensate for the decrease in the number of MGE-derived cortical interneurons. This effect was specific to $reelin^+$ interneurons, which express a common marker even though they derive from different developmental origins. No increase was observed in VIP^+ interneurons, which is consistent with evidence that survival and maturation of this subgroup is not dependent upon activity (Fig. S2C) (De Marco García et al., 2011; Priya et al., 2018).

Decreased inhibitory input onto pyramidal neurons in the cKO cortex

The observed increase in the number of non-MGE-derived upper-layer cortical interneurons does not necessarily imply that these cells can fully compensate for the physiological function of the missing population. We decided to investigate whether the inhibitory input onto excitatory pyramidal cells was altered in the cKO cortex. We performed whole cell electrophysiological recordings in pyramidal neurons located in layers II-III, where we had observed the greatest increase in CGE-derived $reelin^+$ interneurons. We recorded from cells in the cortex of 3-week-old WT and cKO mice, analyzing their inhibitory input by comparing the frequency and amplitude of spontaneous miniature inhibitory postsynaptic currents (mIPSC; Fig. 3A). We found that the frequency of mIPSCs was 33.54% lower in the cKO cortex (Fig. 3B), but their amplitudes were not significantly different (Fig. 3C), consistent with an overall decrease in the number of inhibitory GABAergic inputs. From this, we conclude that the loss of MGE-derived interneurons in the cortex of cKO mice results in a decrease in the inhibitory input to pyramidal neurons in the upper layers that cannot be fully rescued by the increase in the number of upper layer CGE-derived $reelin^+$ interneurons.

Prdm16 regulates MGE progenitor proliferation

We sought to understand the causes leading to the decreased numbers of tdT^+ cortical interneurons in the cortex of cKO mice. One possibility is that defects in the migratory capacity of *Nkx2.1*-lineage interneurons could impair their ability to reach their final destination in the cortex through tangential migration (Anderson et al., 1997; Corbin et al., 2001). We examined the position of tdT^+ interneurons in the developing brains of WT and cKO animals (Fig. S3A), and found no significant differences between them: at E13, tdT^+ cells migrating into the cortex had covered a similar proportion in animals of both genotypes (Fig. S3B), and they had largely occupied the entire cortex by E15 (Fig. S3C). Another possibility is that loss of *Prdm16* function in MGE-derived postmitotic neurons could induce cell death (Close et al., 2012; Denaxa et al., 2012). However, immunostaining for the apoptosis marker cleaved caspase-3 did not differ between WT and cKO cortices at any of the developmental stages analyzed (Fig. S3D).

Development (2020) 147, dev187526. doi:10.1242/dev.187526

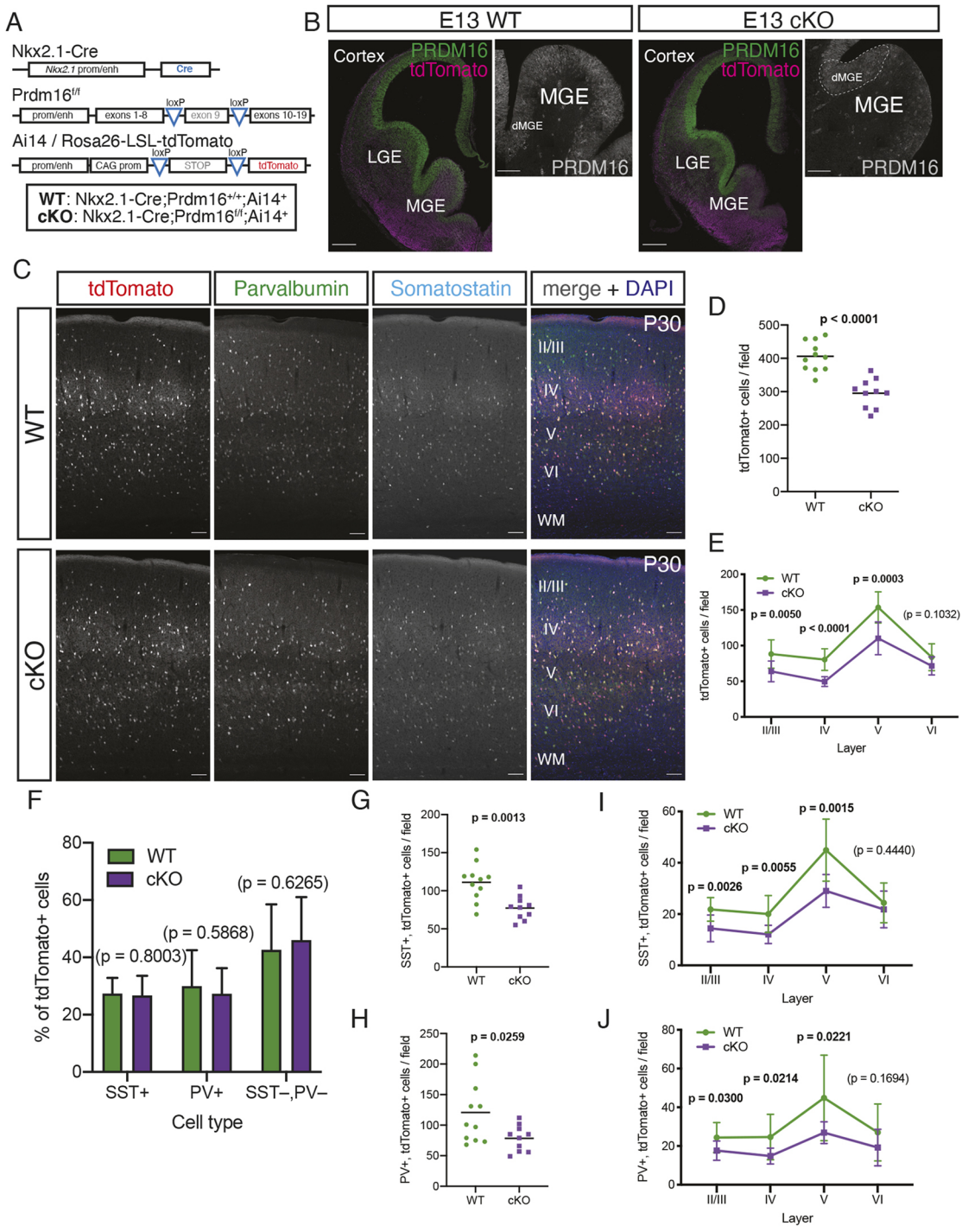

Fig. 1. Deletion of *Prdm16* in the *Nkx2.1* lineage causes a loss of cortical interneurons. (A) Genetic strategy for conditional deletion of *Prdm16* and simultaneous fate mapping of *Nkx2.1*-expressing cells. (B) Left: Overview of a coronal section through one hemisphere of the developing telencephalon, immunostained for PRDM16 (green) and tdT (magenta) at E13 in WT and cKO mice, showing the loss of PRDM16 in the ventricular zone of the *Nkx2.1*-expressing MGE, but not in the lateral ganglionic eminence (LGE) or cortex. Right: Close-up of the MGE of E13 WT and KO embryos, immunostained for PRDM16 (gray); note the presence of PRDM16$^+$ cells in the cKO sample throughout the dorsal domain of the MGE (dMGE, dashed line), where *Nkx2.1* is not expressed. (C) Immunostaining for tdT (red in merged image), PV (green in merge) and SST (cyan in merge), counterstained with DAPI (blue in merge), in the cortex of P30 WT and cKO mice. Cortical layers are indicated in white. (D) Total number of tdT$^+$ cells per 1 mm-wide column spanning the entirety of the cortex. (E) Number of tdT$^+$ cells in each indicated cortical layer, quantified per 1 mm-wide column. (F) Total number of cells co-labeled with SST and tdT (SST$^+$, tdT$^+$) per 1 mm-wide cortical column. (G) Number of SST$^+$, tdT$^+$ cells in each indicated cortical layer, per 1 mm-wide column. (H) Total number of cells co-labeled with PV and tdT (PV$^+$, tdT$^+$) per 1 mm-wide cortical column. (I) Number of PV$^+$, tdT$^+$ cells in each indicated cortical layer, per 1 mm-wide column. Analysis in D-J was performed on samples from P30 WT (green circles) and cKO (purple squares) animals. Black bars in D, G and H indicate the mean. Mean±s.d. is displayed in E, F, I and J. Unpaired *t*-tests with Welch's correction (D,G,H) or multiple *t*-tests (E,F,I,J) were performed; *P*-values are indicated above the corresponding compared sets of data: those highlighted in bold represent significant differences (P<0.05). Scale bars: 250 µm (B, left), 100 µm (B, right; C)

Development (2020) 147, dev187526. doi:10.1242/dev.187526

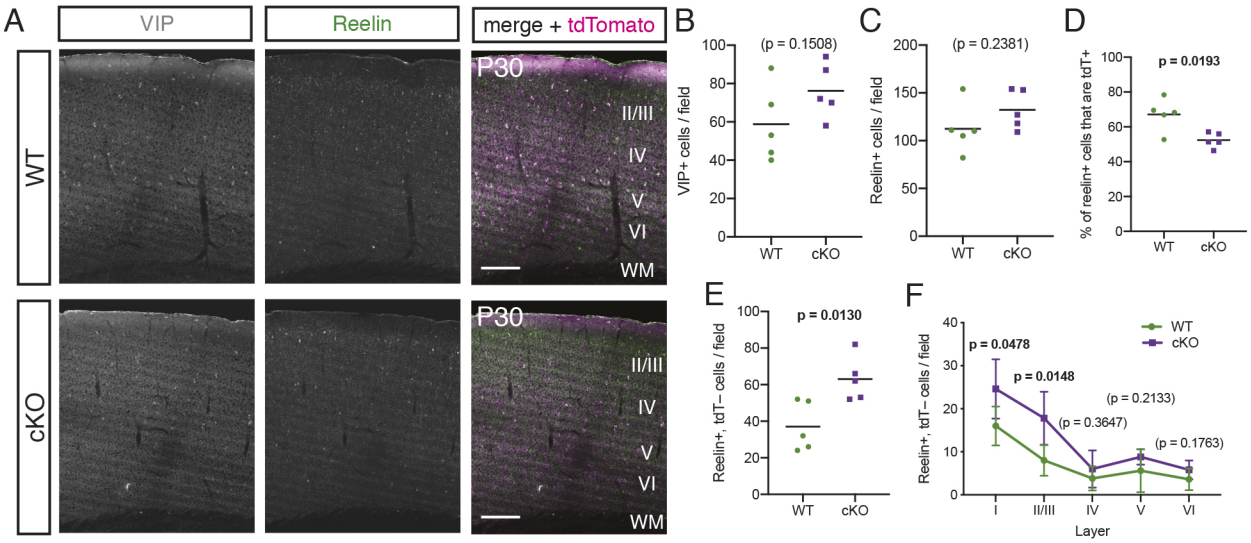

Fig. 2. Loss of *Nkx2.1*-lineage cortical interneurons in *Prdm16* mutants is partially compensated by an increase in non-MGE-derived reelin$^+$ cells in upper layers. (A) Immunostaining for vasointestinal peptide (VIP, green in merge), reelin (gray in merge), and tdT (magenta in merge) in the cortex of P30 WT and cKO mice. Cortical layers are indicated in white. (B) Total number of VIP$^+$ cells per 1 mm-wide column spanning the entirety of the cortex. (C) Total number of reelin$^+$ cells per 1 mm-wide cortical column. (D) Percentage of reelin$^+$ cells co-stained for tdT. (E) Total number of reelin$^+$, tdT$^-$ cells per 1 mm-wide column. (F) Number of reelin$^+$, tdT$^-$ cells in each indicated cortical layer, per 1 mm-wide column. Analysis in B-F was performed on samples from P30 WT (green circles) and cKO (purple squares) animals. Black bars in B-E indicate the mean. Mean±s.d. is displayed in F. Unpaired *t*-tests with Welch's correction (B-E) or multiple *t*-tests (F) were performed; *P*-values are indicated above the corresponding compared sets of data: those highlighted in bold represent significant differences ($P<0.05$). Scale bars: 200 µm.

We conclude that *Prdm16* must exert its role at the progenitor level, guiding the generation of cortical interneurons rather than their survival or long-distance migration.

We analyzed the *Nkx2.1*-expressing progenitors that give rise to these cells. First, we compared the number of progenitors in the MGE of WT and cKO mice at E13, a mid-neurogenic stage (Turrero Garcia and Harwell, 2017). We performed immunofluorescence staining for phosphorylated histone 3 (pH3), a marker of late G2/M phase in cycling cells (Fig. 4A). We found a significant reduction in the overall density of dividing cells in the MGE of cKO mice (Fig. 4B); this effect could be observed both in the ventricular zone (VZ), where radial glia reside (Fig. 4C), and in the subventricular zone (SVZ) (Fig. 4D), which harbors other types of transit-amplifying progenitors (Turrero Garcia and Harwell, 2017). To assess the proliferative capacity of MGE progenitors, we infected embryonic mice with GFP-expressing retrovirus, which allowed us to identify and analyze the progeny (or 'clones') derived from single radial glial cells 24 h after infection (Fig. 4E) (Baizabal et al., 2018; Harwell et al., 2015). Although the majority of clones in the MGE of control mice were composed of two cells, with a smaller proportion of one-cell clones and progressively smaller proportions of bigger clones, in the MGE of cKO mice this distribution was shifted towards smaller clone sizes: almost two-thirds of the clones were composed of a single cell and about one-third of the total were two-cell clones (Fig. 4F). Correspondingly, the average clone size was smaller in the MGE of cKO mice (Fig. 4G). These results indicate that the changes in cortical interneuron output that we observed are the result of defects in the number and proliferative capacity of MGE progenitors.

Prdm16 controls the differentiation of MGE progenitors

We sought to understand better what molecular changes lead to the decreased number and proliferative capacity of progenitors in the MGE of cKO embryos. For this purpose, we performed RNA

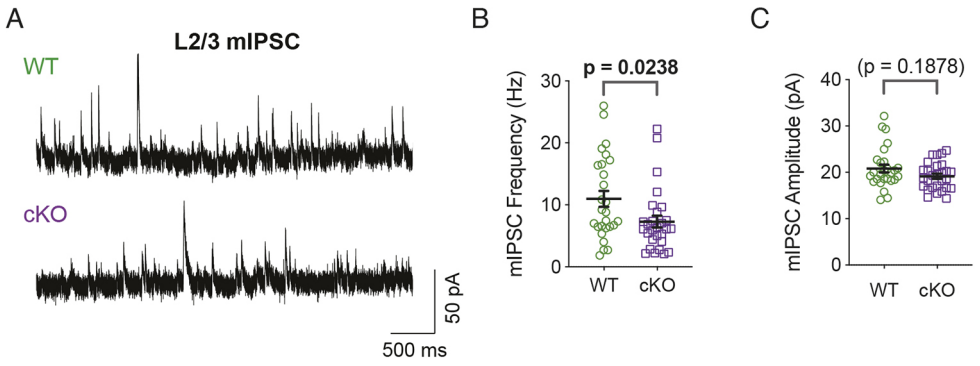

Fig. 3. Pyramidal neurons in the cortex of *Prdm16* mutant mice receive decreased inhibitory inputs. (A) Representative traces of miniature inhibitory postsynaptic currents (mIPSCs) recorded from layer II-III pyramidal cells of the somatosensory cortex of P21 WT and cKO mice. (B,C) Frequency (B) and amplitude (C) values for mIPSCs. For WT (green circles), *N*=3 mice, *n*=27 cells. For cKO mice (purple squares), *N*=3 mice, *n*=28 cells. All values are displayed, with mean±s.e.m. indicated by black bars. Mann–Whitney tests were performed; *P*-values are indicated above the corresponding compared sets of data: the one highlighted in bold represents a significant difference ($P<0.05$).

Development (2020) 147, dev187526. doi:10.1242/dev.187526

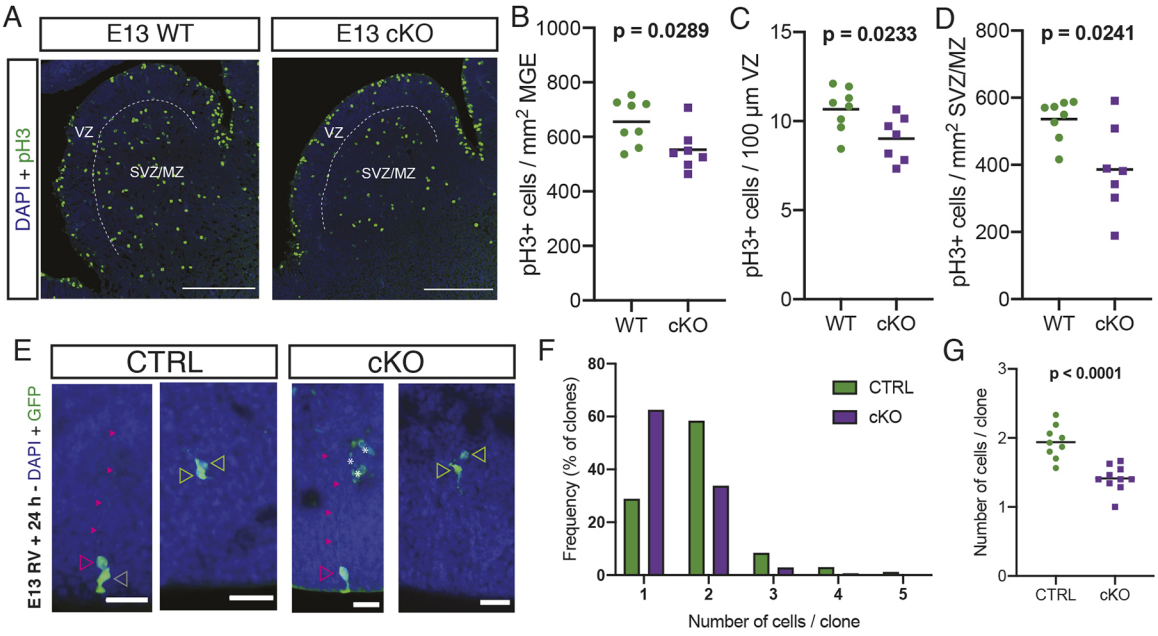

Fig. 4. Loss of cortical interneurons in the cKO cortex is caused by defects in MGE progenitor proliferation. (A) Representative images of immunofluorescence experiments performed on the MGE of WT and cKO mice at E13, stained for the mitotic marker pH3 (green) and tdT (magenta); nuclei were counterstained with DAPI (blue). The VZ and SVZ/MZ are indicated. (B) Quantification of the number of pH3$^+$ cells/mm^2 in the MGE of WT (green circles) and cKO (purple squares) mice at E13. (C) Quantification of the number of VZ pH3$^+$ cells per 100 µm of ventricular surface length in the MGE of WT (green circles) and cKO (purple squares) mice at E13. (D) Quantification of the number of pH3$^+$ cells/mm^2 in the SVZ/MZ of the MGE of WT (green circles) and cKO (purple squares) mice at E13. (E) Representative images of retrovirus-labeled clones in the MGE of WT (left) and cKO (right) mice at 24 h after infection. Clones were typically composed of radial glia (magenta empty arrowheads), distinguished by their long basal processes (small magenta arrowheads) sometimes contacting blood vessels (white asterisks), and/or intermediate progenitors (green empty arrowheads) or other unidentified cells (gray empty arrowhead). (E) Frequency distribution of retrovirally labeled clone size in the MGE of WT (green; *n*=165 clones from 9 embryos) and cKO (purple; *n*=141 clones from 10 embryos) mice at E14, 24 h after infection. (F) Number of cells per MGE clone of WT (green circles) and cKO (purple squares) E14 mice, 24 h after retroviral infection. The average clone sizes for each sample (*n*=9 for WT, *n*=10 for cKO) are represented. Black bars in B-D and G indicate the mean. Unpaired *t*-tests with Welch's correction (B-D,G) were performed; *P*-values are indicated above the corresponding compared sets of data: those highlighted in bold represent significant differences (*P*<0.05). Scale bars: 200 µm (A), 25 µm (E).

sequencing (RNA-Seq) on the dissected MGEs of WT and cKO embryos at E14 (Fig. 5A), comparing three samples of either genotype (Fig. 5B). We found 510 differentially regulated genes (absolute fold change >2, adjusted *P*-value <0.05; see Table S1). Of these, 326 were downregulated in the cKO samples and 184 upregulated (Fig. 5C). Among the downregulated genes (Fig. 5C,D), there are several with known functional roles at various stages of cortical interneuron development, such as *Egfr* (Namba et al., 2017) or *Maf* (Pai et al., 2019); migration, *Erbb4* (Li et al., 2012); and maturation, *Adamts15* (Levy et al., 2015). There are also a number of differentially expressed genes encoding neurotransmitter receptors, such as *Npy1r*, *Htr1a* or *Drd1*. Several of the upregulated genes (Fig. 5C,D) are expressed in MGE radial glia and control their proliferative capacity, as is the case for *Hes5* (Wang et al., 2013) and *Ccnd1* (Glickstein et al., 2007), whereas others control MGE regionalization, such as *Shh* (Xu et al., 2005), *Fgf15* (Danjo et al., 2011) and *Otx2* (Hoch et al., 2015). Overall, these results suggest that the defects we found in cKO mice (Fig. 4) might result from an inability of MGE radial glia to progress correctly through their differentiation program due to the lack of *Prdm16*.

PRDM16 associates with cis-regulatory elements involved in nervous system development

In the cortex, *Prdm16* regulates neurogenesis by modulating the expression of genes involved in the generation of intermediate progenitors and neuronal differentiation (Baizabal et al., 2018). To understand the molecular mechanisms by which *Prdm16* regulates the proliferation and neuronal output of MGE progenitors, we performed chromatin immunoprecipitation followed by sequencing (ChIP-Seq) for PRDM16 on MGE samples isolated from E14 WT mice. We detected 3517 statistically reproducible (IDR *P*<0.05) ChIP-Seq peaks across two experimental replicates, representing PRDM16 binding sites (Table S2). We compared the enrichment of PRDM16 binding sites with those previously characterized in PRDM16 ChIP-Seq experiments performed in E15 cortex (Baizabal et al., 2018). Analysis of all the potential PRDM16 binding sites (Table S3) showed a large overlap between the MGE and cortex datasets (Table S4). To understand more about the epigenetic state of those sites, we compared our list with a published dataset studying histone modifications in the MGE at E13 (Sandberg et al., 2016). Potential PRDM16 binding sites were enriched in open chromatin histone marks H3K4me3, H3K4me1 and H3K27ac, but not in the repressive H3K27me3 modification (Fig. 6A,B). We analyzed the distribution of PRDM16 peaks across the genome and found that the majority of peaks were located in intergenic and intronic genomic regions, whereas about 10% of PRDM16 binding peaks were associated with transcription start sites (TSS) (Fig. 6C). This distribution across genomic regions was enriched in open chromatin marks and similar to that of the E15 cortex dataset (Fig. S4C-E, Fig. S5A) (Baizabal et al., 2018). We then examined the genes closest to MGE PRDM16 peaks by performing gene ontology (GO) analysis. The nearest genes in every annotated genomic region were associated to similar GO terms, with a relative enrichment of terms related to DNA synthesis and repair in genes

Development (2020) 147, dev187526. doi:10.1242/dev.187526

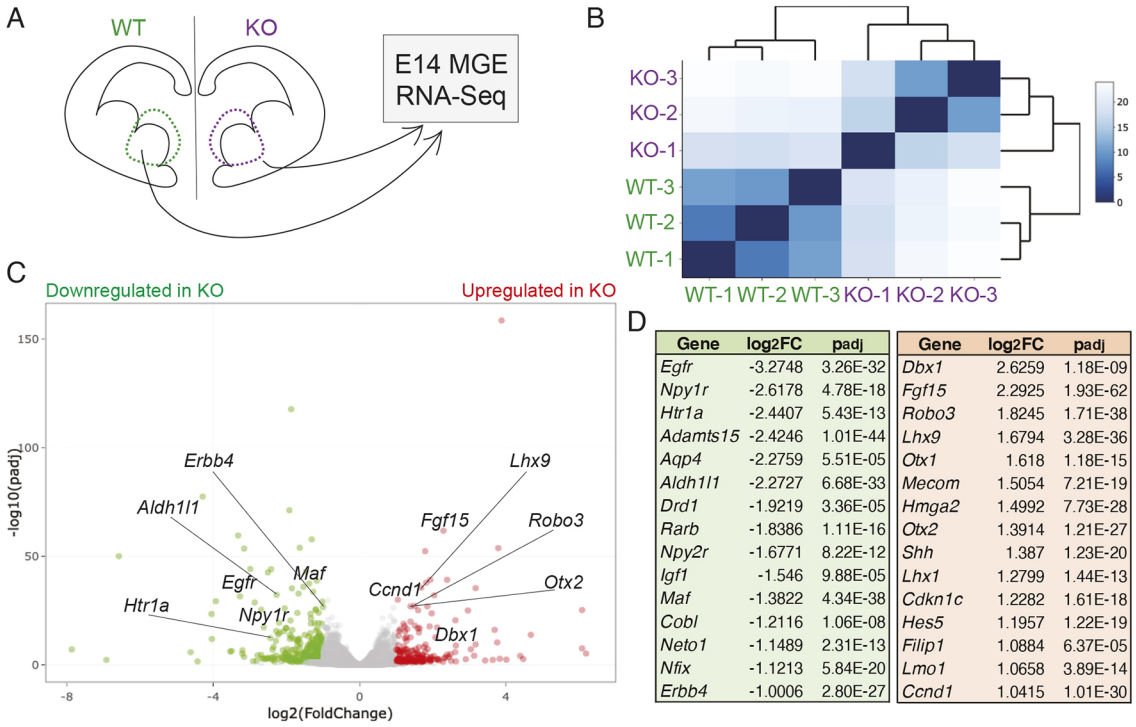

Gene	log2FC	padj
Egfr	-3.2748	3.26E-32
Npy1r	-2.6178	4.78E-18
Htr1a	-2.4407	5.43E-13
Adamts15	-2.4246	1.01E-44
Aqp4	-2.2759	5.51E-05
Aldh1l1	-2.2727	6.68E-33
Drd1	-1.9219	3.36E-05
Rarb	-1.8386	1.11E-16
Npy2r	-1.6771	8.22E-12
Igf1	-1.546	9.88E-05
Maf	-1.3822	4.34E-38
Cobl	-1.2116	1.06E-08
Neto1	-1.1489	2.31E-13
Nfix	-1.1213	5.84E-20
Erbb4	-1.0006	2.80E-27

Gene	log2FC	padj
Dbx1	2.6259	1.18E-09
Fgf15	2.2925	1.93E-62
Robo3	1.8245	1.71E-38
Lhx9	1.6794	3.28E-36
Otx1	1.618	1.18E-15
Mecom	1.5054	7.21E-19
Hmga2	1.4992	7.73E-28
Otx2	1.3914	1.21E-27
Shh	1.387	1.23E-20
Lhx1	1.2799	1.44E-13
Cdkn1c	1.2282	1.61E-18
Hes5	1.1957	1.22E-19
Filip1	1.0884	6.37E-05
Lmo1	1.0658	3.89E-14
Ccnd1	1.0415	1.01E-30

Fig. 5. *Prdm16* controls the expression of genes involved in MGE progenitor differentiation. (A) Schematic of the experiment: the MGEs of E14 WT or cKO mice were dissected out and subjected to RNA sequencing. (B) Heatmap representing the similarity between samples (as measured by their Euclidean distance; more saturated colors represent higher similarity) and their hierarchical clustering. (C) Volcano plot displaying genes down- (green) or upregulated (red) in cKO samples compared to WT. Several example genes are highlighted. (D) Lists of example down- and upregulated genes in cKO with respect to WT.

close to TSS-associated peaks (Fig. S4B). All of the top 30 GO terms for genes were related to developmental processes, including the generation and migration of neurons (Fig. 6D). We compared the MGE and cortex ChIP-Seq datasets to find out which PRDM16 peaks were exclusive to MGE progenitors. We generated a list of highly enriched peaks (greater than threefold enrichment over input) for both datasets and obtained a list of 3206 peaks. When we analyzed the regional specificity of those peaks (Fig. 6E), we found that about one-third of them were unique to the MGE (Table S5), two-thirds were common to both datasets (Table S4) and less than 10% were cortex specific (Table S6). GO terms of nearest genes for both subsets of peaks had overall similar representation, with a slightly lower representation of synaptic signaling-related terms in MGE-exclusive peaks (Fig. S5B).

It is possible that PRDM16 exhibits lineage-specific genomic binding in order to direct GABAergic versus glutamatergic cell fate specification. To explore this possibility, we analyzed the sequence of PRDM16 peaks, searching for *de novo* or known binding motifs either in all MGE peaks (Fig. 6F) or in the MGE-specific subset (Fig. 6G). MGE peaks that overlapped with cortical peaks were enriched in binding motifs for transcriptional regulators associated with neurogenesis, including LHX2 and SOX10 (Chou and Tole, 2019; Weider and Wegner, 2017). MGE-exclusive peaks showed motif enrichment for TCF12 and ASCL1, which are basic helix-loop-helix (bHLH) transcription factors involved in progenitor proliferation and neuronal cell fate determination (Dennis et al., 2019). We compared the binding sites of PRDM16 in the MGE that we obtained in this study and those of ASCL1 obtained from an *in vitro* model (Castro et al., 2011) and found 127 overlapping peaks, several of which were associated with genes that control progenitor identity (Table S7). Together, these data suggest that PRDM16 forms MGE-specific complexes with transcription factors known to regulate genetic programs guiding the specification of cortical interneurons (Sandberg et al., 2018). We cross-compared the list of 510 differentially regulated genes from our RNA-Seq experiment (Fig. 5) with the lists of PRDM16 ChIP-Seq peaks in the cortex (Baizabal et al., 2018) and the MGE in order to identify genes that could be potential direct targets of PRDM16. We identified a total of 75 genes that were associated with PRDM16 binding sites; 50 of them contained peaks that were common to the MGE and cortex, 21 contained only MGE-exclusive peaks and 4 displayed peaks unique to the cortex (Fig. 6H). This suggests that PRDM16 exerts its gene regulatory functions through both common and unique sites between the MGE and the cortex.

PRDM16 downregulates neuronal differentiation genes

To understand the function of PRDM16 *in vivo*, we selected two genes that contained PRDM16 ChIP-Seq peaks: *Pdzrn3* and *Lmo1*. Several ChIP-Seq peaks in the *Pdzrn3* genomic locus were common to the MGE and cortex datasets (Fig. 7A). We previously showed that *Pdzrn3* repression by PRDM16 controls the migration of pyramidal neurons in the cortex (Baizabal et al., 2018). A ChIP-Seq peak in the *Lmo1* genomic locus was exclusive to the MGE (Fig. 7B). *Lmo1* is a direct target of *Arx*, a gene essential for basal forebrain development (Fulp et al., 2008), and has been proposed to play a role in cortical interneuron development (Friocourt and Parnavelas, 2011) but its specific function in this context is still unknown. To understand how PRDM16 binding controls cortical interneuron specification through *Pdzrn3* and *Lmo1*, we compared the expression levels of these genes in the MGE of WT and cKO mice at E13. We directly visualized the spatial pattern of *Pdzrn3* and *Lmo1* expression using single molecule fluorescent *in situ* hybridization (RNAscope) on embryonic tissue sections of WT and cKO embryos. We detected RNA puncta representing single

Development (2020) 147, dev187526. doi:10.1242/dev.187526

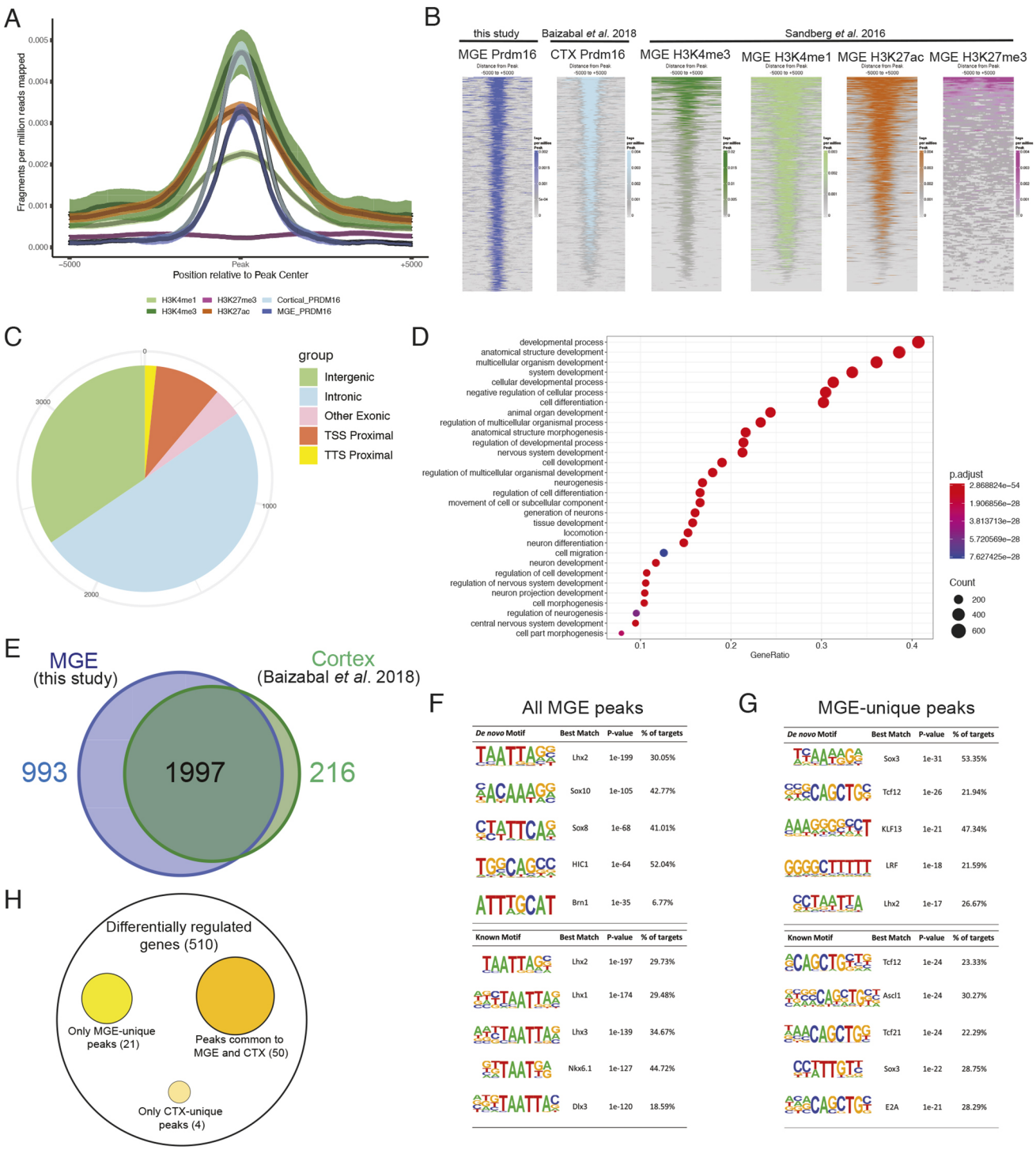

Fig. 6. PRDM16 binding sites in the MGE are associated with open chromatin marks and genes implicated in neural development. (A) Read density (fragments per million reads mapped) in several embryonic ChIP-Seq experiments (color-coded as explained in B), within a genomic window centered around PRDM16 binding sites in the embryonic cortex (light blue) or the MGE (all other plots). (B) Heatmap representation of the read density around PRDM16 binding sites for the ChIP-Seq experiments depicted in A (each line in a heatmap represents an individual PRDM16 binding site); data were generated for this study from the E14 MGE (dark blue) or obtained from Baizabal et al. (2018) (CTX; ChIP-Seq for PRDM16 in E15 cortex; light blue) and Sandberg et al. (2016) (ChIP-Seq for each specified histone modification in E13 MGE; all other plots). (C) Genome-wide distribution of E13 MGE PRDM16 ChIP-Seq peaks relative to gene annotations (TSS: transcription start site; TTS: transcription termination site). (D) Gene ontology term enrichment in potential PRDM16 binding sites in the MGE, obtained by analysis of genes closest to ChIP-Seq peaks. (E) Overlap of PRDM16 peaks between cortex and MGE ChIP-Seq experiments. The number of peaks within each sector of the Venn diagram is indicated. (F,G) *De novo* (top) and known (bottom) motif analysis of PRDM16 ChIP-Seq peaks, in all MGE peaks (F) or MGE-exclusive peaks (G). (H) Venn diagram representing the proportion of differentially regulated genes in the MGE of *Prdm16* cKO mice (as identified by RNA-Seq; see Fig. 5 and Tables S2-S6) with PRDM16 ChIP-Seq peaks either exclusive to the MGE (yellow) or the cortex (light orange) or common to both (dark orange).

Development (2020) 147, dev187526. doi:10.1242/dev.187526

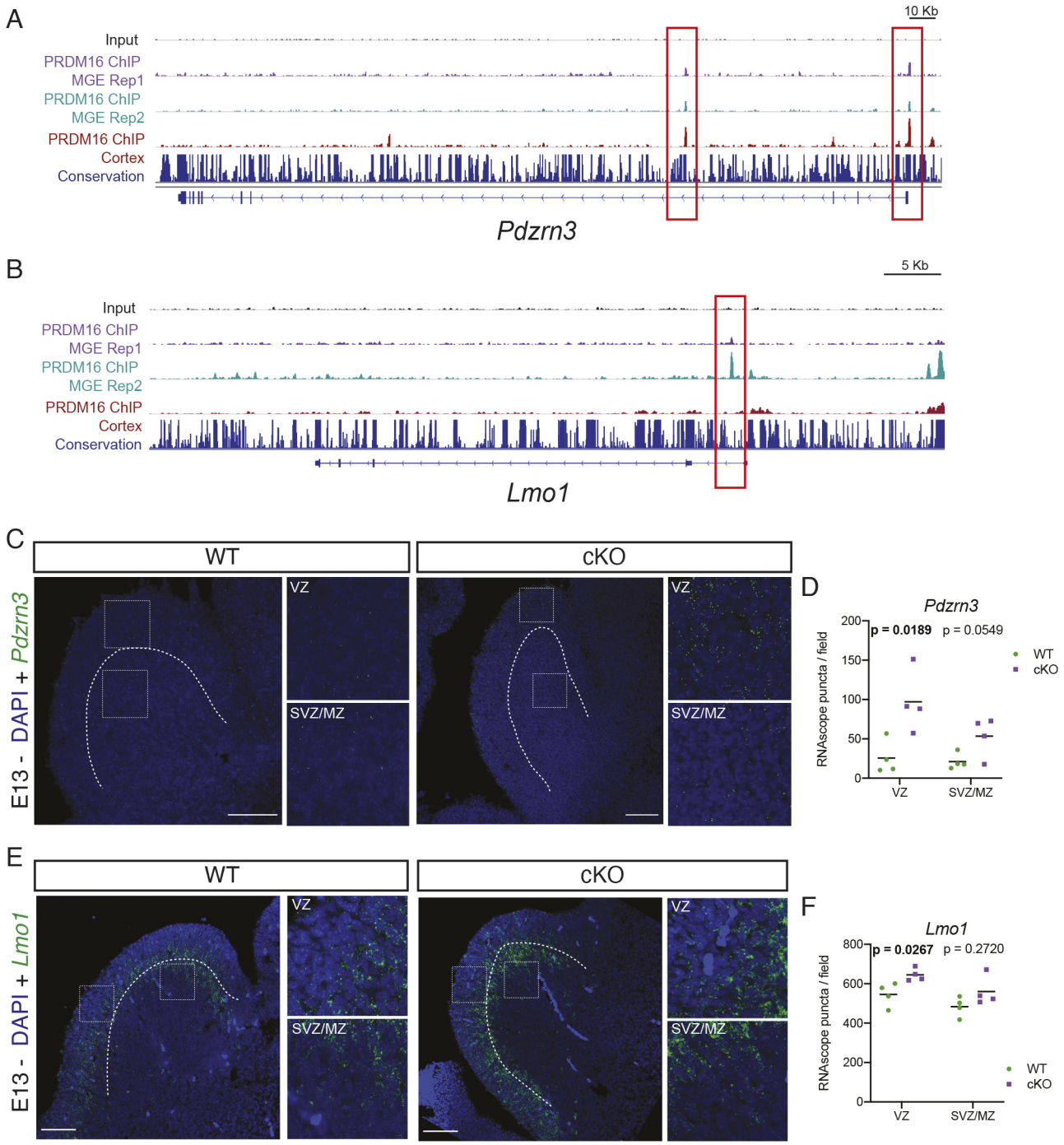

Fig. 7. PRDM16 represses the expression of genes involved in neuronal differentiation in the MGE. (A,B) ChIP-Seq tracks showing PRDM16 binding sites in two ChIP-Seq experimental replicates in the E14 MGE (middle tracks), compared to E15 cortex (bottom track), in the loci of *Pdzrn3* (A) and *Lmo1* (B). Input (top track); genomic conservation (dark blue, bottom) is shown for comparison. Detected ChIP-Seq peaks common to MGE and cortex (*Pdzrn3*) or unique to the MGE (*Lmo1*) are highlighted by red boxes. (C,E) Images from *in situ* hybridization experiments for *Pdzrn3* (C) or *Lmo1* (E) transcripts (green) in the MGE of WT and cKO embryos at E13, counterstained with DAPI (blue). Dotted lines indicate the border between VZ and SVZ/MZ. Dotted boxes are shown magnified on the right and display example 100×100 µm images from the VZ and SVZ/MZ, as indicated. (D,F) Quantification of the average number of *Pdzrn3* (D) or *Lmo1* (F) RNA puncta per field of view, as obtained by *in situ* hybridization in the VZ and SVZ/MZ of WT and cKO embryos at E13 (n=4 embryos for both WT and cKO). Black bars indicate the mean. Multiple *t*-tests (D,F) were performed; *P*-values are indicated above the corresponding compared sets of data: those highlighted in bold represent significant differences (P<0.05). Scale bars: 100 µm.

mRNA transcripts of either *Pdzrn3* (Fig. 7C) or *Lmo1* (Fig. 7E). Automated quantification of these puncta in the VZ and subventricular/mantle zone (SVZ/MZ) revealed that there was a significant increase in the expression levels of both genes in cKO animals that was specific to the VZ in both cases (Fig. 7D,F). This suggests that PRDM16 primarily acts in VZ radial glia to repress the expression of genes involved in neuronal differentiation, thus allowing these cells to maintain their proliferative capacity and transition through transit-amplifying stages in order to generate sufficient numbers of cortical interneurons.

Development (2020) 147, dev187526. doi:10.1242/dev.187526

DISCUSSION

Prdm16 is expressed in radial glia in all telencephalic proliferative zones, suggesting that it might play a key role in the specification of most forebrain neuron lineages (Baizabal et al., 2018; Chuikov et al., 2010; Inoue et al., 2017; Shimada et al., 2017). In the cortex, PRDM16 binds to developmental enhancers involved in the specification and migration of upper layer pyramidal neurons, and promotes indirect neurogenic divisions of RG and production of transit-amplifying intermediate progenitors (Baizabal et al., 2018). Here we show that loss of *Prdm16* in MGE progenitors leads to a decrease in their proliferation and to a reduction in interneuron numbers in the cortex and hippocampus; however, in contrast to the cortical *Prdm16* mutant phenotype, this reduction is not layer- or neuronal subtype-specific (Fig. 1; Fig. S1). The decrease in MGE-derived interneurons is not caused by an increased rate of developmental cell death or to an altered pattern of tangential migration within this population (Fig. S3), but rather to defects in the proliferation of *Nkx2.1*-expressing progenitors (Fig. 4). We observed both a reduction in the number of dividing progenitors and a decrease in their proliferative capacity, as evidenced by the smaller size of retrovirus-labeled clones in the mutant MGE. Because the retroviral genome is only transmitted to one of the two daughter cells in radial glia divisions (Cepko et al., 1995), and given the fact that the viral genome can be silenced (Halliday and Cepko, 1992), our clone analysis experiments probably underestimate the actual size of clones derived from the infected progenitors. However, this should be the case for both the control and experimental samples, so we believe the interpretation of the data is clear: MGE progenitors have a lower proliferative capacity in the brain of cKO mice. This might be due to a number of reasons, including alterations in their cell cycle dynamics (such as cell cycle length), changes in the division mode of radial glia and/or the presence of different types of progenitors in the mutant MGE (Glickstein et al., 2009; Petros et al., 2015; Pilz et al., 2013; Ross, 2011). The loss of both early- and late-born neuronal lineages from the MGE could reflect key differences in the general role that transit-amplifying progenitors might play in different proliferative regions: in the cortex they have been shown to be the main source of upper-layer pyramidal neurons (Mihalas et al., 2016), but their contribution to the neuronal output of the MGE is still largely unexplored. Different subtypes of transit-amplifying MGE progenitors are biased towards the generation of PV^+ and SST^+ cortical interneurons (Petros et al., 2015), but it is unknown whether transit-amplifying cells are required throughout the entire neurogenic period. Based on our results, we propose that the majority of MGE-derived interneurons are generated through a transit-amplifying progenitor; the decreased ability of radial glia to transition into this type of progenitor in *Prdm16* mutants is reflected by the uniform loss of interneurons across cortical layers and between both histological subgroups. In the future, it will be important to determine the fate potential and diversity of transit-amplifying progenitors throughout the neurogenic period for GABAergic cortical interneurons (Kelly et al., 2019 preprint).

The vast majority of cortical interneurons are derived from two distinct ventral telencephalic sources, the MGE and CGE (Wonders and Anderson, 2006). In our study, the loss of MGE-derived interneurons in mutant cortices appears to be partially compensated by an increase in the number of interneurons from a CGE-derived population (Fig. 2). This is in line with previous research (Denaxa et al., 2018), suggesting a homeostatic mechanism for setting interneuron numbers in response to network activity within the developing cortex. Our electrophysiological recordings demonstrate that a compensatory increase in the number of CGE-derived interneurons was not enough to restore inhibitory inputs onto cortical pyramidal cells to wild-type levels (Fig. 3). This is probably due to the specific circuit and functional features of $reelin^+$ interneurons, which cannot fill in for the inhibitory circuit functions of PV and SST subgroups derived from the MGE (Olah et al., 2007; Pesold et al., 1999). This suggests that maintaining the proper number and diverse complement of cortical interneuron subgroups derived from different developmental sources is necessary to maintain inhibitory balance (Denaxa et al., 2018).

Numerous studies have investigated the roles of different gene expression programs in the specification of cortical interneurons from MGE progenitors (Nord et al., 2015). Our work adds to this growing body of knowledge by identifying a series of genes whose expression is controlled by *Prdm16* (Fig. 5; Tables S1, S8). Overall, the functions of these genes support the idea that *Prdm16* promotes the generation of cortical interneurons by guiding MGE radial glia through progressively more differentiative divisions, including the production of transit-amplifying progenitors. In the future, it will be important to determine how *Prdm16*-regulated genes in the MGE control the proliferative capacity and fate potential of different progenitor subtypes to produce the right number and complement of cortical interneuron types.

In both the MGE and the developing cortex, PRDM16 binds to cis-regulatory elements in the genome and prevents premature neuronal differentiation by repressing neuronal maturation genes (Figs 6, 7; Figs S4, S5) (Baizabal et al., 2018). This is consistent with the observation that PRDM16 binds to a largely overlapping set of distal regulatory elements associated with marks of open chromatin in both MGE and cortical progenitors (Fig. 6). We also found a number of overlapping genes containing PRDM16 binding sites in a recent ChIP-Seq dataset obtained from the entire heads of E13 mice (He et al., 2019 preprint) (Table S8). Just as in the cortex, *Prdm16* repressor function in the MGE might serve to ensure proper timing of lineage-specific gene expression programs to ensure timely transitions from radial glia into transit-amplifying progenitors, which in turn would be responsible for the generation of sufficient numbers of cortical interneurons.

Although many common aspects of cortical and MGE progenitor function probably require overlapping networks of genes, there are fundamental differences in the migratory capacity and neurotransmitter identity of their neuronal progeny. How might PRDM16 contribute to lineage-specific differentiation programs? In the case of genes that are bound by PRDM16 in both cortical and MGE progenitors, such as *Pdzrn3*, which encodes an E3 ubiquitin ligase-RING domain containing protein, the molecular function of the encoded protein could be conserved, but the cellular response might be different, eliciting distinct effects on cell fate determination in each proliferative region. This would be consistent with the prominent role that this gene plays in the radial migration of pyramidal cells in the neocortex (Baizabal et al., 2018), although the migratory capacity of MGE-derived interneurons does not appear to be affected in *Prdm16* cKO brains (Fig. S3A-C).

It is also very likely that PRDM16 regulates lineage-specific differentiation programs through associations to genomic loci that are exclusive to MGE progenitors (Fig. 6H). It is notable that MGE-specific PRDM16-bound genomic regions are enriched for sequence motifs of bHLH family transcription factors such as ASCL1, which is expressed exclusively in ventral telencephalic neural progenitors and is known to regulate GABAergic neuron specification (Long et al., 2009). We found that PRDM16 associated with genomic loci previously shown to be bound by ASCL1. Although it is important to note that the ASCL1 data was derived from an *in vitro* model, the significant overlap suggests the potential for *in vivo* interactions between PRDM16 and ASCL1 in the MGE (Table S7). Many bHLH transcription factors such as OLIG2, ASCL1 and NeuroD family

Development (2020) 147, dev187526. doi:10.1242/dev.187526

members are expressed exclusively in either ventral or dorsal progenitors (Casarosa et al., 1999; Lu et al., 2000; Osorio et al., 2010). Prdm family members have been shown to interact with bHLH transcription factors (Hohenauer and Moore, 2012; Kinameri et al., 2008; Ross et al., 2012), which are in many cases crucial for proper neuronal production by neural progenitors, both in the dorsal and the ventral telencephalon. It has been proposed that interactions between Prdm family proteins and bHLH transcription factors is a conserved mechanism for the regulation of gene expression during neural development (Hohenauer and Moore, 2012; Ross et al., 2012). Such transcription factor complexes may function in the proliferative zones where they are expressed in order to direct differentiation and lineage progression programs towards region-specific neuronal subtype specification (Lindtner et al., 2019). Our genomic analysis of PRDM16 binding in MGE progenitors sheds light on the lineage-specific transcriptional programs regulated by PRDM16 and suggests that specialized PRDM16-associated protein complexes orchestrate these programs in different progenitor types.

In humans, the *PRDM16* gene is located in a distal critical region of chromosome 1 that is deleted in 1p36 deletion syndrome (Jordan et al., 2015). Patients affected by this condition exhibit a spectrum of clinical features that includes intellectual disability, developmental delay and epileptic seizures. It is still unknown to what extent this phenotype is caused by the deletion of PRDM16, but it is likely that distinct mechanisms underlie each of its different clinical aspects. Our study begins to unravel the important question of how PRDM16 controls the fate of progenitors by regulating specific transcriptional programs necessary for neuronal fate determination and excitatory and inhibitory circuit development.

MATERIALS AND METHODS

Experimental model and subject details

All animal procedures conducted in this study followed experimental protocols approved by the Institutional Animal Care and Use Committee of Harvard Medical School. Mouse lines are listed in Table S9. Mouse housing and husbandry conditions were performed in accordance with the standards of the Harvard Medical School Center of Comparative Medicine. Mice were group housed in a 12 h light/dark cycle, with access to food and water *ad libitum*. Samples were obtained from animals at embryonic days E13, E14 and E17 and postnatal days P0, P7, P14, P21 and P30, as indicated in the figure legends. All results reported in adult (P30) and late postnatal stages (P14, P21) include animals of both sexes; the sex of embryos and animals at early postnatal stages was not determined.

Tissue processing

Postnatal animals were transcardially perfused with PBS followed by 4% paraformaldehyde (PFA) in 120 mM phosphate buffer; their brains were dissected out and post-fixed in 4% PFA for 2-4 h at room temperature or overnight at 4°C. Brains were sectioned into 75-100 µm sections on a vibratome (Leica Microsystems VT1200S) and either further processed for immunofluorescence staining or stored at 4°C in PBS containing 0.05% sodium azide. Embryonic brains were dissected out in ice-cold PBS and fixed in 4% PFA for 2-4 h at room temperature or overnight at 4°C. Their brains were cryoprotected in 30% sucrose in PBS overnight at 4°C, embedded in OCT compound (Sakura), frozen and stored at −20°C. Samples were sectioned at 20 µm on a cryostat (Thermo Fisher CryoStar NX70); sections were either stored at −20°C or further processed for immunofluorescence staining. For fresh frozen samples (used for fluorescent *in situ* hybridization; FISH), the brains were extracted in PBS and immediately embedded in OCT compound, then frozen on dry ice.

Immunofluorescence staining

Floating vibratome sections

Samples were permeabilized with 0.5% Triton X-100 (Amresco) in PBS for 1-2 h and blocked in blocking buffer (10% goat serum, 0.1% Triton X-100 in PBS) for 1-2 h at room temperature. The sections were then incubated for 24-72 h with primary antibodies diluted in blocking buffer at 4°C. The samples were washed three times (10-30 min/wash) with PBS, counterstained with DAPI (4′,6-diamidino-phenylindole; Invitrogen) for 45 min (both steps at room temperature), and incubated with secondary antibodies diluted in blocking buffer for 2 h at room temperature or overnight at 4°C. Samples were then washed (three 10-30 min washes) and mounted on slides with ProLong Gold Antifade Mountant (Invitrogen).

Cryosections

Slides were allowed to reach room temperature and then washed three times with PBS. Sections were permeabilized with 0.5% Triton X-100 in PBS for 30 min and blocked with blocking buffer for 1 h at room temperature. Slides were incubated with primary antibodies diluted in blocking buffer overnight, in a humid chamber at 4°C. They were then washed with PBS (three 10-30 min washes), counterstained with DAPI (45 min), and incubated for 1-2 h with secondary antibodies diluted in blocking buffer, at room temperature. Slides were washed (three 10-30 min washes) with PBS and mounted with ProLong Gold Antifade Mountant.

Imaging and image analysis

Images were acquired using either a Leica DM5500B wide field microscope or a Leica SP8 laser point scanning confocal microscope. Objectives of 10×, 20× and 25× magnification were used, and the parameters of image acquisition (speed, resolution, averaging, zoom, z-stack, etc.) were adjusted for each set of samples. Images were further analyzed using ImageJ, both in its native and Fiji distributions, as described below. Brightness and contrast were adjusted as necessary for visualization, but the source images were kept unmodified.

Migration analysis

Embryonic samples from medial regions of the neocortex, immunostained for tdT and counterstained with DAPI, were used. The length of the cortex was measured from the pallial/subpallial boundary (PSB) between the lateral ganglionic eminence (LGE) and the developing cortex to the start of the cortical hem, through the center of the tissue [set as the basal end of the SVZ at E13, and the SVZ-intermediate zone (IZ) boundary at E15]. The position of the cell soma closest to the cortical hem was taken as the furthest point of migration; its distance to the PSB was measured, divided by the total length of the cortex and presented as a percentage. Where available, this measurement was repeated across both hemispheres of each sample.

Acute slice preparation and electrophysiology

Mice (19-21 days old) were anesthetized by isoflurane inhalation and perfused transcardially with ice-cold artificial cerebrospinal fluid (ACSF) containing (in mM): 125 NaCl, 2.5 KCl, 25 $NaHCO_3$, 2 $CaCl_2$, 1 $MgCl_2$, 1.25 NaH_2PO_4 plus 25 glucose and 310 mOsm/kg. Cerebral hemispheres were removed and sliced in cold ACSF (300 µm coronal slices on a Leica VT1200S vibratome). Coronal slices containing somatosensory cortex were recovered for 15-20 min at 34°C in choline-based recovery solution (in mM): 110 choline chloride, 25 $NaHCO_3$, 2.5 KCl, 7 $MgCl_2$, 0.5 $CaCl_2$, 1.25 NaH_2PO_4, 25 glucose, 11.6 ascorbic acid and 3.1 pyruvic acid, and then transferred to a holding chamber with 34°C ACSF that progressively cooled down to room temperature (20-22°C). All recordings were obtained within 1-6 h after slicing and solutions were constantly bubbled with 95% O_2 and 5% CO_2. Individual slices were transferred to a recording chamber mounted on an upright microscope (Olympus BX51WI) and continuously perfused (1-2 ml/min) with ACSF at room temperature. Cells were visualized using a 40× water-immersion objective with infrared DIC optics. Whole-cell voltage-clamp recordings (room temperature) were made from pyramidal cells in L2/3 somatosensory cortex. Patch pipettes (2-4 MΩ) pulled from borosilicate glass (BF150-86-7.5, Sutter Instruments) were filled with a Cs^+-based internal solution containing (in mM) 130 $CsMeSO_4$, 10 HEPES, 1.8 $MgCl_2$, 4 Na_2ATP, 0.3 NaGTP, 8 Na_2-phosphocreatine, 10 $CsCl_2$ and 3.3 QX-314 (Cl^- salt), pH 7.3 adjusted with CsOH, plus 295 mOsm/kg. For all voltage-clamp experiments, errors due to voltage drop across the series resistance (<20 MOhm) were left uncompensated. To isolate mIPSCs, cells

Development (2020) 147, dev187526. doi:10.1242/dev.187526

were held at −0 mV and ACSF included 20 µM NBQX (Tocris), 10 µM (R)-CPP (Tocris) and 1 µM Tetrodotoxin (Sigma). Membrane currents were amplified and low-pass filtered at 3 kHz using a Multiclamp 700B amplifier (Molecular Devices), digitized at 10 kHz and acquired using National Instruments acquisition boards and a custom version of ScanImage written in MATLAB (Mathworks). Off-line analysis of mIPSC frequency was performed using custom routines written in MATLAB and Igor Pro (Wavemetrics). Statistical analyses were done in GraphPad Prism 7 software (GraphPad).

Viral production and *in utero* injection

The retrovirus packaging cell line HEK293 gp NIT-GFP was grown to 90% confluence in DMEM supplemented with 10% fetal bovine serum. Cells were transfected with a pCMV-VSV-G vector using Lipofectamin 2000 (Invitrogen) and Optimem (Gibco). Two days after transfection, the cell supernatant was collected, filtered through a 0.45 µm filter (VWR International) and centrifuged at 25,000 rpm (~80,000 ***g***) for 90 min at 4°C. After discarding the supernatant, 100 µl of cold PBS+Ca^{2+} was added to the pellet, which was incubated overnight at 4°C. Viral particles were then resuspended, aliquoted and stored at −80°C. The titer of the viral preparation was determined to be 10^6-10^7 cfu. Timed pregnant mice were anesthetized using an isoflurane vaporizer and placed on a warming pad. An abdominal incision (approximately 2 cm wide) was made, and the uterine horns were exposed on top of a sterile gauze pad. The uterus was periodically moistened with sterile PBS prewarmed at 37°C during the entire procedure. Approximately 0.5-1 µl of retrovirus, mixed with 0.05% Fast Green for visualization, was injected into the lateral ventricles of each embryo using heat-pulled beveled glass micropipettes (Drummond). The abdominal cavity was sutured and stapled before administering buprenorphine (0.05-0.1 mg/kg) and ketoprofen (5-10 mg/kg). The pregnant dams were allowed to recover in a 35°C chamber for 1-2 h after surgery, then returned to usual housing conditions and sacrificed 24 h after surgery; the embryos were retrieved and processed as explained above.

RNA-sequencing

The MGEs of E14 embryos were manually dissected out and flash-frozen with liquid nitrogen. After confirming the genotype of each embryo, three samples (i.e. six MGEs) were pooled for each experimental replicate (three WT and three KO pools). Tissue digestion, RNA extraction and sequencing and bioinformatic analyses were conducted by GENEWIZ (South Plainfield, NJ). After RNA extraction, sequencing reads (42-71 million reads/sample) were obtained in an Illumina HiSeq sequencer. Reads were trimmed to remove possible adapter sequences and nucleotides with poor quality using Trimmomatic v.0.36. The trimmed reads were mapped to the *Mus musculus* GRCm38 reference genome available on ENSEMBL using the STAR aligner v.2.5.2b. Unique gene hit counts were calculated using featureCounts from the Subread package v.1.5.2. The hit counts were summarized and reported using the gene_id feature in the annotation file. Only unique reads that fell within exon regions were counted. After extraction of gene hit counts, the gene hit counts table was used for downstream differential expression analysis. Using DESeq2, a comparison of gene expression between the defined groups of samples (WT versus KO) was performed. The Wald test was used to generate *P*-values and $\log_2$ fold changes. Genes with an adjusted *P*-value <0.05 and absolute $\log_2$ fold change >1 were considered differentially expressed genes for each comparison.

Chromatin immunoprecipitation and sequencing

The MGE of 18 embryos from two litters of E14 WT mice were dissected out and finely minced. Cells were dual crosslinked by incubating in 1.5 mM EGS (ethylene glycol bis[succinimidyl succinate]) solution for 20 min with rotation, and then with 1% PFA and 1.5 mM EGS for an additional 10 min (both steps were performed at room temperature). Crosslinking was quenched by adding glycine to a final concentration of 125 mM and rotating for 5 min at room temperature. Cells were then washed twice with cold PBS containing EDTA-free protease inhibitor, centrifuged and stored at −80°C or freshly resuspended in lysis buffer (20 mM Tris-HCl pH 8.0, 85 mM KCl, 0.5% NP40) and incubated on ice for 30 min. Nuclei were pelleted by centrifugation at 1500 ***g*** for 5 min, resuspended in SDS buffer (0.2% SDS, 20 mM Tris-HCl pH 8.0, 1 mM EDTA) and incubated on ice for 10 min. Nuclei were then sonicated using a Covaris S2 ultrasonicator for shearing chromatin into fragments with a size range of 100-500 bp. After spinning chromatin at 18,000 ***g*** for 10 min, supernatant was transferred to a clean tube and one volume of 2× ChIP dilution buffer (0.1% sodium deoxycholate, 2% Triton X-100, 2 mM EDTA, 30 mM Tris-HCl pH 8.0, 300 mM NaCl) was added. At this step, a volume of supernatant containing around 0.5 million nuclei was set aside as input control and the remaining supernatant was incubated with 5 mg of anti-PRDM16 antibody overnight at 4°C with rotation. Next day, 50 ml of washed protein G beads (22.5 mg/ml; Novex) were added to the chromatin solution and incubated for 2 h at 4°C. After incubation, beads were washed twice with low salt wash buffer (0.1% SDS, 1% Triton X-100, 2 mM EDTA, 20 mM Tris-HCl pH 8.0, 150 mM NaCl) followed by two washes with high salt wash buffer (0.1% SDS, 1% Triton X-100, 2 mM EDTA, 20 mM Tris-HCl pH 8.0, 500 mM NaCl) then two washes with LiCl wash buffer (0.25 M LiCl, 0.5% NP40, 0.5% sodium deoxycholate, 1 mM EDTA, 10 mM Tris-HCl pH 8.0) and finally two washes with TE pH 8.0 (10 mM Tris-HCl, 1 mM EDTA). Beads were then resuspended in 90 ml of freshly prepared ChIP elution buffer (1% SDS, 0.1 M $NaHCO_3$) and incubated at 65°C for 30 min with rotation. The recovered supernatant was incubated in reverse crosslinking solution (250 mM Tris-HCl pH 6.5, 62.5 mM EDTA pH 8.0, 1.25 M NaCl, 5 mg/ml Proteinase K) at 65°C overnight. DNA was then extracted with phenol/chloroform/isoamyl alcohol, precipitated with 3 M sodium acetate pH 5.0 and resuspended in TE pH 8.0 low EDTA (10 mM Tris-HCl, 0.1 mM EDTA). Finally, samples were treated with RNase A (100 mg/ml) for 30 min at 37°C. For library preparation, genomic DNA was purified, end repaired, ligated with barcoded adapters, amplified for 14 PCR cycles and purified using the Ovation Ultralow System V2 (NuGEN) according to the manufacturer's instructions. Library fragments in the range of 100-800 bp were size-selected using agarose gel electrophoresis followed by DNA gel extraction (Qiagen). Recovered DNA was further cleaned and concentrated using a column (Zymo Research). Libraries were sequenced in an Illumina HiSeq 2500 sequencer to a sequencing depth of 30-40 million reads per sample.

ChIP-Seq analysis

Reference genomic sequence and annotations for the mouse genome (mm10) were obtained from the University of California Santa Cruz Genomics Institute (Casper et al., 2018). ChIP-Seq reads generated from PRDM16 ChIP and input libraries were aligned to the mouse genome using bowtie2 (Langmead and Salzberg, 2012) with default parameters except for '-I 50 -X 750'. The read densities were calculated with the Gaussian kernel (bandwidth of 35 bp) using the R package SPP (Kharchenko et al., 2008). Peaks were called using MACS2 (version 2.1.2) (Zhang et al., 2008) with 'callpeak' and a *P*-value threshold of 0.05 followed by irreproducible discovery rate (IDR) analysis, as described by Landt et al. (2012), with a threshold of ≤0.05. The MGE peak set was compared to the previously published cortical PRDM16 ChIP experiment (Baizabal et al., 2018), with a merged set of peaks defined by the union of the MGE and cortical peak sets. Peaks were considered to be present in both cortical and MGE samples if the ChIP/input ratio of library-size normalized read counts within the peak region was ≥3 for both experiments. Peaks were considered 'cortical only' ('MGE only') if the ChIP/input ratio was ≥3 for the cortical (MGE) experiment and ≤1.5 for the MGE (cortical) experiment. Gene ontology enrichment analysis was performed using the R package ClusterProfiler (Yu et al., 2012) with the parameters ont='BP' and maxGSSize=20,000.

Motif analysis was performed on set peaks detected in the MGE using HOMER (Heinz et al., 2010). *De novo* motif analysis was conducted by parsing input sequences at ±100 bp from peak center. The FDR-corrected probability of that motif being over-represented amongst target sequences is presented as a *q*-value. Known motif enrichment was screened against the JASPAR database of previously determined high quality motifs.

Fluorescent *in situ* hybridization

Fresh frozen or PFA-fixed samples (see above) were submitted to the RNAscope protocol (Advanced Cell Diagnostics), following

the manufacturer's instructions. RNAscope probes against each transcript (see Table S9) were purchased from ACD. In each experiment, probes against the candidate gene were used in combination with a *tdTomato* probe to confirm that all areas analyzed were within the portion of the MGE where *Nkx2.1*-Cre-mediated recombination had taken place.

Cell quantification

The CellCounter tool in ImageJ or Fiji was used for all cell quantifications. In the mature cortex (Fig. 1C-J, Fig. 2A-J), 1 mm-wide sections were selected from images obtained at the level of the somatosensory cortex. All cells positive for the markers analyzed in each case were quantified within each cortical layer, as identified by the distribution of DAPI-counterstained nuclei. In the hippocampus (Fig. S1A-H), the entire structure was analyzed at equivalent rostro-caudal levels; layers and areas were determined by the distribution of DAPI-counterstained nuclei. In the striatum and nucleus accumbens (Fig. S1I,J), 500×500 µm squares were drawn in the same regions within these structures, at equivalent rostro-caudal levels, and numbers were normalized by square millimeter. In the developing cortex at different stages (Fig. 3A), the entire surface of the neocortex was measured on both hemispheres of each sample at equivalent rostro-caudal levels, and the number of cells positive for CC3 and tdT was quantified within the measured surface, then normalized by square millimeter. In E13 MGE samples (Fig. 3B), the entire surface of the MGE in sections at equivalent rostro-caudal locations was measured; cells positive for pH3 were quantified within the measured area and normalized by square millimeter. For the quantification of MGE clones (Fig. 3D-F), cells were considered as part of the same clone if they had similar fluorescence intensities and were located within 50 µm of the radial fiber in the case of RG-containing clones or within a 50 µm radius in the case of IP-containing clones. Clones were not analyzed if other GFP-labeled cells of different fluorescence intensity were present in their vicinity (within 100 µm of the radial fiber or within a 100 µm radius). Quantification of RNA puncta per area was performed using an automated data processing pipeline in MatLab, guided by MatBots (https://hms-idac.github.io/MatBots); each data point corresponds to the average values from the analysis of three fields (dimensions: 100×100 µm or 50×50 µm) selected within the VZ and SVZ/MZ of two sections or MGEs per sample (where available; in some cases, only one section could be analyzed). Cell and RNA puncta numbers were compiled in Microsoft Excel spreadsheets; GraphPad Prism 8 (GraphPad) was used to build graphs.

Statistical analysis

All statistical analyses were performed with GraphPad Prism 8, as detailed in the figure legends. All *P*-values were rounded to four decimal places, and are presented above each statistical comparison in the corresponding figures; those highlighted in bold are below 0.05, which was considered the cut-off for statistical significance (*P*-values deemed not statistically significant under this criterion are displayed in parenthesis above the corresponding comparisons in the figures).

Acknowledgements

The authors thank Patrick Seale and Jeremy Dasen for their generous gift of anti-PRDM16 antibodies; Bernardo Sabatini for providing equipment and resources for the electrophysiology experiments; Mahmoud El-Rifai and Aurélien Begué at the Neurobiology Imaging Facility at Harvard Medical School for performing RNAscope experiments; Steve Vu for technical support; all members of the Harwell, Goodrich, Lehtinen and Segal labs for discussions and comments; and A. Denise Garcia, Rebecca Ihrie and Debby Silver for their comments on the manuscript.

Competing interests

The authors declare no competing or financial interests.

Author contributions

Conceptualization: C.C.H., M.T.G.; Formal analysis: M.A.A., M.A.B., M.Y.T.; Investigation: M.T.G., J.-M.B., D.N.T., R.P., W.W., Y.X., M.A.A., L.A.E., C.M.R., S.I.B., M.A.B., M.Y.T.; Resources: C.C.H.; Data curation: M.T.G., M.A.A.; Writing - original draft: C.C.H., M.T.G.; Writing - review & editing: C.C.H., M.T.G., J.-M.B., D.N.T., R.P., Y.X., M.A.A.; Visualization: M.T.G., M.A.A., M.A.B., M.Y.T.; Supervision: C.C.H.; Funding acquisition: C.C.H.

Funding

M.T.G. was partially supported by the Ellen R. and Melvin J. Gordon Center for the Cure and Treatment of Paralysis. Research in C.C.H.'s laboratory is supported by the National Institutes of Health (R01MH119156 and R01NS102228) and by a Harvard Brain Science Initiative Seed Grant. C.M.R. and S.I.B. are working under the Harvard PhD Program in Neuroscience. Deposited in PMC for release after 12 months.

Data availability

Data from RNA-seq and PRDM16 ChIP-seq experiments were deposited in GEO under accession number GSE159730.

Supplementary information

Supplementary information available online at
https://dev.biologists.org/lookup/doi/10.1242/dev.187526.supplemental

Peer review history

The peer review history is available online at
https://dev.biologists.org/lookup/doi/10.1242/dev.187526.reviewer-comments.pdf

References

Anderson, S. A., EisenstatD. D., Shi, L. and Rubenstein, J. L. (1997). Interneuron migration from basal forebrain to neocortex: dependence on Dlx genes. *Science* **278**, 474-476. doi:10.1126/science.278.5337.474

Anthony, T. E., Klein, C., Fishell, G. and Heintz, N. (2004). Radial glia serve as neuronal progenitors in all regions of the central nervous system. *Neuron* **41**, 881-890. doi:10.1016/S0896-6273(04)00140-0

Baizabal, J. M., Mistry, M., Garcia, M. T., Gomez, N., Olukoya, O., Tran, D., Johnson, M. B., Walsh, C. A. and Harwell, C. C. (2018). The epigenetic state of PRDM16-regulated enhancers in radial glia controls cortical neuron position. *Neuron* **98**, 945-962.e8. doi:10.1016/j.neuron.2018.04.033

Campbell, K. (2003). Dorsal-ventral patterning in the mammalian telencephalon. *Curr. Opin. Neurobiol.* **13**, 50-56. doi:10.1016/S0959-4388(03)00009-6

Casarosa, S., Fode, C. and Guillemot, F. (1999). Mash1 regulates neurogenesis in the ventral telencephalon. *Development* **126**, 525-534.

Casper, J., Zweig, A. S., Villarreal, C., Tyner, C., Speir, M. L., Rosenbloom, K. R., Raney, B. J., Lee, C. M., Lee, B. T., Karolchik, D., et al. (2018). The UCSC Genome Browser database: 2018 update. *Nucleic Acids Res.* **46**, D762-D769. doi:10.1093/nar/gkx1020

Castro, D. S., Martynoga, B., Parras, C., Ramesh, V., Pacary, E., Johnston, C., Drechsel, D., Lebel-Potter, M., Garcia, L. G., Hunt, C. et al. (2011). A novel function of the proneural factor Ascl1 in progenitor proliferation identified by genome-wide characterization of its targets. *Genes Dev.* **25**, 930-945. doi:10.1101/gad.627811

Cepko, C., Ryder, E. F., Austin, C. P., Walsh, C. and Fekete, D. M. (1995). Lineage analysis using retrovirus vectors. *Methods Enzymol.* **254**, 387-419. doi:10.1016/0076-6879(95)54027-X

Chou, S.-J. and Tole, S. (2019). Lhx2, an evolutionarily conserved, multifunctional regulator of forebrain development. *Brain Res.* **1705**, 1-14. doi:10.1016/j.brainres.2018.02.046

Chuikov, S., Levi, B. P., Smith, M. L. and Morrison, S. J. (2010). Prdm16 promotes stem cell maintenance in multiple tissues, partly by regulating oxidative stress. *Nat. Cell Biol.* **12**, 999-1006. doi:10.1038/ncb2101

Close, J., Xu, H., De Marco Garcia, N., Batista-Brito, R., Rossignol, E., Rudy, B. and Fishell, G. (2012). Satb1 is an activity-modulated transcription factor required for the terminal differentiation and connectivity of medial ganglionic eminence-derived cortical interneurons. *J. Neurosci.* **32**, 17690-17705. doi:10.1523/JNEUROSCI.3583-12.2012

Cohen, P., Levy, J. D., Zhang, Y., Frontini, A., Kolodin, D. P., Svensson, K. J., Lo, J. C., Zeng, X., Ye, L., Khandekar, M. J. et al. (2014). Ablation of PRDM16 and beige adipose causes metabolic dysfunction and a subcutaneous to visceral fat switch. *Cell* **156**, 304-316. doi:10.1016/j.cell.2013.12.021

Corbin, J. G., Nery, S. and Fishell, G. (2001). Telencephalic cells take a tangent: non-radial migration in the mammalian forebrain. *Nat. Neurosci.* **4 Suppl**, 1177-1182. doi:10.1038/nn749

Danjo, T., Eiraku, M., Muguruma, K., Watanabe, K., Kawada, M., Yanagawa, Y., Rubenstein, J. L. and Sasai, Y. (2011). Subregional specification of embryonic stem cell-derived ventral telencephalic tissues by timed and combinatory treatment with extrinsic signals. *J. Neurosci.* **31**, 1919-1933. doi:10.1523/JNEUROSCI.5128-10.2011

De Marco García, N. V., Karayannis, T. and Fishell, G. (2011). Neuronal activity is required for the development of specific cortical interneuron subtypes. *Nature* **472**, 351-355. doi:10.1038/nature09865

Denaxa, M., Kalaitzidou, M., Garefalaki, A., Achimastou, A., Lasrado, R., Maes, T. and Pachnis, V. (2012). Maturation-promoting activity of SATB1 in MGE-derived cortical interneurons. *Cell Rep.* **2**, 1351-1362. doi:10.1016/j.celrep.2012.10.003

Denaxa, M., Neves, G., Rabinowitz, A., Kemlo, S., Liodis, P., Burrone, J. and Pachnis, V. (2018). Modulation of Apoptosis Controls Inhibitory Interneuron Number in the Cortex. *Cell Rep.* **22**, 1710-1721. doi:10.1016/j.celrep.2018.01.064

Dennis, D. J., Han, S. and Schuurmans, C. (2019). bHLH transcription factors in neural development, disease, and reprogramming. *Brain Res.* **1705**, 48-65. doi:10.1016/j.brainres.2018.03.013

Friocourt, G. and Parnavelas, J. G. (2011). Identification of Arx targets unveils new candidates for controlling cortical interneuron migration and differentiation. *Front. Cell Neurosci.* **5**, 28. doi:10.3389/fncel.2011.00028

Fulp, C. T., Cho, G., Marsh, E. D., Nasrallah, I. M., Labosky, P. A. and Golden, J. A. (2008). Identification of Arx transcriptional targets in the developing basal forebrain. *Hum. Mol. Genet.* **17**, 3740-3760. doi:10.1093/hmg/ddn271

Glickstein, S. B., Moore, H., Slowinska, B., Racchumi, J., Suh, M., Chuhma, N. and Ross, M. E. (2007). Selective cortical interneuron and GABA deficits in cyclin D2-null mice. *Development* **134**, 4083-4093. doi:10.1242/dev.008524

Glickstein, S. B., Monaghan, J. A., Koeller, H. B., Jones, T. K. and Ross, M. E. (2009). Cyclin D2 is critical for intermediate progenitor cell proliferation in the embryonic cortex. *J. Neurosci.* **29**, 9614-9624. doi:10.1523/JNEUROSCI.2284-09.2009

Govindan, S. and Jabaudon, D. (2017). Coupling progenitor and neuronal diversity in the developing neocortex. *FEBS Lett.* **591**, 3960-3977. doi:10.1002/1873-3468.12846

Halliday, A. L. and Cepko, C. L. (1992). Generation and migration of cells in the developing striatum. *Neuron* **9**, 15-26. doi:10.1016/0896-6273(92)90216-Z

Harwell, C. C., Fuentealba, L. C., Gonzalez-Cerrillo, A., Parker, P. R., Gertz, C. C., Mazzola, E., Garcia, M. T., Alvarez-Buylla, A., Cepko, C. L. and Kriegstein, A. R. (2015). Wide Dispersion and Diversity of Clonally Related Inhibitory Interneurons. *Neuron* **87**, 999-1007. doi:10.1016/j.neuron.2015.07.030

He, L., Jones, J., He, W., Bjork, B., Wen, J. and Dai, Q. (2019). PRDM16 establishes lineage-specific transcriptional program to promote temporal progression of neural progenitors in the mouse neocortex. bioRxiv, 573857. doi 10.1101/573857

Heinz, S., Benner, C., Spann, N., Bertolino, E., Lin, Y. C., Laslo, P., Cheng, J. X., Murre, C., Singh, H. and Glass, C. K. (2010). Simple combinations of lineage-determining transcription factors prime cis-regulatory elements required for macrophage and B cell identities. *Mol. Cell* **38**, 576-589. doi:10.1016/j.molcel.2010.05.004

Hoch, R. V., Lindtner, S., Price, J. D. and Rubenstein, J. L. (2015). OTX2 Transcription Factor Controls Regional Patterning within the Medial Ganglionic Eminence and Regional Identity of the Septum. *Cell Rep* **12**, 482-494. doi:10.1016/j.celrep.2015.06.043

Hohenauer, T. and Moore, A. W. (2012). The Prdm family: expanding roles in stem cells and development. *Development* **139**, 2267-2282. doi:10.1242/dev.070110

Hu, J. S., Vogt, D., Sandberg, M. and Rubenstein, J. L. (2017). Cortical interneuron development: a tale of time and space. *Development* **144**, 3867-3878. doi:10.1242/dev.132852

Inoue, M., Iwai, R., Tabata, H., Konno, D., Komabayashi-Suzuki, M., Watanabe, C., Iwanari, H., Mochizuki, Y., Hamakubo, T., Matsuzaki, F. et al. (2017). Prdm16 is crucial for progression of the multipolar phase during neural differentiation of the developing neocortex. *Development* **144**, 385-399. doi:10.1242/dev.136382

Jordan, V. K., Zaveri, H. P. and Scott, D. A. (2015). 1p36 deletion syndrome: an update. *Appl. Clin. Genet.* **8**, 189-200.

Kelly, S. M., Raudales, R., Moissidis, M., Kim, G. and Huang, Z. J. (2019). Multipotent radial glia progenitors and fate-restricted intermediate progenitors sequentially generate diverse cortical interneuron types. bioRxiv, 735019. doi:10.1101/735019

Kharchenko, P. V., Tolstorukov, M. Y. and Park, P. J. (2008). Design and analysis of ChIP-seq experiments for DNA-binding proteins. *Nat. Biotechnol.* **26**, 1351. doi:10.1038/nbt.1508

Kinameri, E., Inoue, T., Aruga, J., Imayoshi, I., Kageyama, R., Shimogori, T. and Moore, A. W. (2008). Prdm proto-oncogene transcription factor family expression and interaction with the Notch-Hes pathway in mouse neurogenesis. *PLoS One* **3**, e3859. doi:10.1371/journal.pone.0003859

Landt, S. G., Marinov, G. K., Kundaje, A., Kheradpour, P., Pauli, F., Batzoglou, S., Bernstein, B. E., Bickel, P., Brown, J. B., Cayting, P. et al. (2012). ChIP-seq guidelines and practices of the ENCODE and modENCODE consortia. *Genome Res.* **22**, 1813-1831. doi:10.1101/gr.136184.111

Langmead, B. and Salzberg, S. L. (2012). Fast gapped-read alignment with Bowtie 2. *Nat. Methods* **9**, 357. doi:10.1038/nmeth.1923

Lee, S., Hjerling-Leffler, J., Zagha, E., Fishell, G. and Rudy, B. (2010). The largest group of superficial neocortical GABAergic interneurons expresses ionotropic serotonin receptors. *J. Neurosci.* **30**, 16796-16808. doi:10.1523/JNEUROSCI.1869-10.2010

Levy, C., Brooks, J. M., Chen, J., Su, J. and Fox, M. A. (2015). Cell-specific and developmental expression of lectican-cleaving proteases in mouse hippocampus and neocortex. *J. Comp. Neurol.* **523**, 629-648. doi:10.1002/cne.23701

Li, H., Chou, S.-J., Hamasaki, T., Perez-Garcia, C. G. and O'Leary, D. D. (2012). Neuregulin repellent signaling via ErbB4 restricts GABAergic interneurons to migratory paths from ganglionic eminence to cortical destinations. *Neural Dev.* **7**, 10. doi:10.1186/1749-8104-7-10

Lim, L., Mi, D., Llorca, A. and Marin, O. (2018). Development and Functional Diversification of Cortical Interneurons. *Neuron* **100**, 294-313. doi:10.1016/j.neuron.2018.10.009

Lindtner, S., Catta-Preta, R., Tian, H., Su-Feher, L., Price, J. D., Dickel, D. E., Greiner, V., Silberberg, S. N., McKinsey, G. L., McManus, M. T. et al. (2019). Genomic Resolution of DLX-Orchestrated Transcriptional Circuits Driving Development of Forebrain GABAergic Neurons. *Cell Rep.* **28**, 2048-2063e2048.

Long, J. E., Swan, C., Liang, W. S., Cobos, I., Potter, G. B. and Rubenstein, J. L. (2009). Dlx1&2 and Mash1 transcription factors control striatal patterning and differentiation through parallel and overlapping pathways. *J. Comp. Neurol.* **512**, 556-572. doi:10.1002/cne.21854

Lopez-Bendito, G., Sturgess, K., Erdelyi, F., Szabo, G., Molnar, Z. and Paulsen, O. (2004). Preferential origin and layer destination of GAD65-GFP cortical interneurons. *Cereb. Cortex* **14**, 1122-1133. doi:10.1093/cercor/bhh072

Lu, Q. R., Yuk, D., Alberta, J. A., Zhu, Z., Pawlitzky, I., Chan, J., McMahon, A. P., Stiles, C. D. and Rowitch, D. H. (2000). Sonic hedgehog–regulated oligodendrocyte lineage genes encoding bHLH proteins in the mammalian central nervous system. *Neuron* **25**, 317-329. doi:10.1016/S0896-6273(00)80897-1

Madisen, L., Zwingman, T. A., Sunkin, S. M., Oh, S. W., Zariwala, H. A., Gu, H., Ng, L. L., Palmiter, R. D., Hawrylycz, M. J., Jones, A. R. et al. (2010). A robust and high-throughput Cre reporting and characterization system for the whole mouse brain. *Nat. Neurosci.* **13**, 133-140. doi:10.1038/nn.2467

Marin, O. and Muller, U. (2014). Lineage origins of GABAergic versus glutamatergic neurons in the neocortex. *Curr. Opin. Neurobiol.* **26**, 132-141. doi:10.1016/j.conb.2014.01.015

Mihalas, A. B., Elsen, G. E., Bedogni, F., Daza, R. A. M., Ramos-Laguna, K. A., Arnold, S. J. and Hevner, R. F. (2016). Intermediate Progenitor Cohorts Differentially Generate Cortical Layers and Require Tbr2 for Timely Acquisition of Neuronal Subtype Identity. *Cell Rep.* **16**, 92-105. doi:10.1016/j.celrep.2016.05.072

Miyoshi, G., Butt, S. J. B., Takebayashi, H. and Fishell, G. (2007). Physiologically distinct temporal cohorts of cortical interneurons arise from telencephalic Olig2-expressing precursors. *J. Neurosci.* **27**, 7786-7798. doi:10.1523/JNEUROSCI.1807-07.2007

Miyoshi, G., Hjerling-Leffler, J., Karayannis, T., Sousa, V. H., Butt, S. J., Battiste, J., Johnson, J. E., Machold, R. P. and Fishell, G. (2010). Genetic fate mapping reveals that the caudal ganglionic eminence produces a large and diverse population of superficial cortical interneurons. *J. Neurosci.* **30**, 1582-1594. doi:10.1523/JNEUROSCI.4515-09.2010

Namba, H., Nagano, T., Jodo, E., Eifuku, S., Horie, M., Takebayashi, H., Iwakura, Y., Sotoyama, H., Takei, N. and Nawa, H. (2017). Epidermal growth factor signals attenuate phenotypic and functional development of neocortical GABA neurons. *J. Neurochem.* **142**, 886-900. doi:10.1111/jnc.14097

Nery, S., Fishell, G. and Corbin, J. G. (2002). The caudal ganglionic eminence is a source of distinct cortical and subcortical cell populations. *Nat. Neurosci.* **5**, 1279-1287. doi:10.1038/nn971

Neves, G., Shah, M. M., Liodis, P., Achimastou, A., Denaxa, M., Roalfe, G., Sesay, A., Walker, M. C. and Pachnis, V. (2013). The LIM homeodomain protein Lhx6 regulates maturation of interneurons and network excitability in the mammalian cortex. *Cereb. Cortex* **23**, 1811-1823. doi:10.1093/cercor/bhs159

Nord, A. S., Pattabiraman, K., Visel, A. and Rubenstein, J. L. (2015). Genomic perspectives of transcriptional regulation in forebrain development. *Neuron* **85**, 27-47. doi:10.1016/j.neuron.2014.11.011

Olah, S., Komlosi, G., Szabadics, J., Varga, C., Toth, E., Barzo, P. and Tamas, G. (2007). Output of neurogliaform cells to various neuron types in the human and rat cerebral cortex. *Front Neural Circuits* **1**, 4. doi:10.3389/neuro.04.004.2007

Osorio, J., Mueller, T., Retaux, S., Vernier, P. and Wullimann, M. F. (2010). Phylotypic expression of the bHLH genes Neurogenin2, Neurod, and Mash1 in the mouse embryonic forebrain. *J. Comp. Neurol.* **518**, 851-871. doi:10.1002/cne.22247

Pai, E. L., Vogt, D., Clemente-Perez, A., McKinsey, G. L., Cho, F. S., Hu, J. S., Wimer, M., Paul, A., Fazel Darbandi, S., Pla, R. et al. (2019). Mafb and c-Maf Have Prenatal Compensatory and Postnatal Antagonistic Roles in Cortical Interneuron Fate and Function. *Cell Rep.* **26**, 1157-1173e1155.

Palmer, T. D., Markakis, E. A., Willhoite, A. R., Safar, F. and Gage, F. H. (1999). Fibroblast growth factor-2 activates a latent neurogenic program in neural stem cells from diverse regions of the adult CNS. *J. Neurosci.* **19**, 8487-8497. doi:10.1523/JNEUROSCI.19-19-08487.1999

Pesold, C., Liu, W. S., Guidotti, A., Costa, E. and Caruncho, H. J. (1999). Cortical bitufted, horizontal, and Martinotti cells preferentially express and secrete reelin into perineuronal nets, nonsynaptically modulating gene expression. *Proc. Natl. Acad. Sci. U.S.A.* **96**, 3217-3222. doi:10.1073/pnas.96.6.3217

Petros, T. J., Bultje, R. S., Ross, M. E., Fishell, G. and Anderson, S. A. (2015). Apical versus Basal Neurogenesis Directs Cortical Interneuron Subclass Fate. *Cell Rep.* **13**, 1090-1095. doi:10.1016/j.celrep.2015.09.079

Petryniak, M. A., Potter, G. B., Rowitch, D. H. and Rubenstein, J. L. (2007). Dlx1 and Dlx2 control neuronal versus oligodendroglial cell fate acquisition in the developing forebrain. *Neuron* **55**, 417-433. doi:10.1016/j.neuron.2007.06.036

Pilz, G.-A., Shitamukai, A., Reillo, I., Pacary, E., Schwausch, J., Stahl, R., Ninkovic, J., Snippert, H. J., Clevers, H., Godinho, L. et al. (2013). Amplification of progenitors in the mammalian telencephalon includes a new radial glial cell type. *Nat. Commun.* **4**, 2125. doi:10.1038/ncomms3125

Priya, R., Paredes, M. F., Karayannis, T., Yusuf, N., Liu, X., Jaglin, X., Graef, I., Alvarez-Buylla, A. and Fishell, G. (2018). Activity Regulates Cell Death within Cortical Interneurons through a Calcineurin-Dependent Mechanism. *Cell Rep.* **22**, 1695-1709. doi:10.1016/j.celrep.2018.01.007

Ross, M. E. (2011). Cell cycle regulation and interneuron production. *Dev. Neurobiol.* **71**, 2-9. doi:10.1002/dneu.20823

Ross, S. E., McCord, A. E., Jung, C., Atan, D., Mok, S. I., Hemberg, M., Kim, T.-K., Salogiannis, J., Hu, L., Cohen, S. et al. (2012). Bhlhb5 and Prdm8 form a repressor complex involved in neuronal circuit assembly. *Neuron* **73**, 292-303. doi:10.1016/j.neuron.2011.09.035

Sandberg, M., Flandin, P., Silberberg, S., Su-Feher, L., Price, J. D., Hu, J. S., Kim, C., Visel, A., Nord, A. S. and Rubenstein, J. L. R. (2016). Transcriptional Networks Controlled by NKX2-1 in the Development of Forebrain GABAergic Neurons. *Neuron* **91**, 1260-1275. doi:10.1016/j.neuron.2016.08.020

Sandberg, M., Taher, L., Hu, J., Black, B. L., Nord, A. S. and Rubenstein, J. L. R. (2018). Genomic analysis of transcriptional networks directing progression of cell states during MGE development. *Neural Dev.* **13**, 21. doi:10.1186/s13064-018-0119-4

Schindelin, J., Arganda-Carreras, I., Frise, E., Kaynig, V., Longair, M., Pietzsch, T., Preibisch, S., Rueden, C., Saalfeld, S., Schmid, B. et al. (2012). Fiji: an open-source platform for biological-image analysis. *Nat. Methods* **9**, 676-682. doi:10.1038/nmeth.2019

Schneider, C. A., Rasband, W. S. and Eliceiri, K. W. (2012). NIH Image to ImageJ: 25 years of image analysis. *Nat. Methods* **9**, 671-675. doi:10.1038/nmeth.2089

Shimada, I. S., Acar, M., Burgess, R. J., Zhao, Z. and Morrison, S. J. (2017). Prdm16 is required for the maintenance of neural stem cells in the postnatal forebrain and their differentiation into ependymal cells. *Genes Dev.* **31**, 1134-1146. doi:10.1101/gad.291773.116

Southwell, D. G., Nicholas, C. R., Basbaum, A. I., Stryker, M. P., Kriegstein, A. R., Rubenstein, J. L. and Alvarez-Buylla, A. (2014). Interneurons from embryonic development to cell-based therapy. *Science* **344**, 1240622. doi:10.1126/science.1240622

Turrero Garcia, M. and Harwell, C. C. (2017). Radial glia in the ventral telencephalon. *FEBS Lett.* **591**, 3942-3959. doi:10.1002/1873-3468.12829

Wang, B., Long, J. E., Flandin, P., Pla, R., Waclaw, R. R., Campbell, K. and Rubenstein, J. L. (2013). Loss of Gsx1 and Gsx2 function rescues distinct phenotypes in Dlx1/2 mutants. *J. Comp. Neurol.* **521**, 1561-1584. doi:10.1002/cne.23242

Weider, M. and Wegner, M. (2017). SoxE factors: Transcriptional regulators of neural differentiation and nervous system development. *Semin. Cell Dev. Biol.* **63**, 35-42. doi:10.1016/j.semcdb.2016.08.013

Wilson, S. W. and Rubenstein, J. L. (2000). Induction and dorsoventral patterning of the telencephalon. *Neuron* **28**, 641-651. doi:10.1016/S0896-6273(00)00171-9

Wonders, C. P. and Anderson, S. A. (2006). The origin and specification of cortical interneurons. *Nat. Rev. Neurosci.* **7**, 687-696. doi:10.1038/nrn1954

Xu, Q., Cobos, I., De La Cruz, E., Rubenstein, J. L. and Anderson, S. A. (2004). Origins of cortical interneuron subtypes. *J. Neurosci.* **24**, 2612-2622. doi:10.1523/JNEUROSCI.5667-03.2004

Xu, Q., Wonders, C. P. and Anderson, S. A. (2005). Sonic hedgehog maintains the identity of cortical interneuron progenitors in the ventral telencephalon. *Development* **132**, 4987-4998. doi:10.1242/dev.02090

Xu, Q., Tam, M. and Anderson, S. A. (2008). Fate mapping Nkx2.1-lineage cells in the mouse telencephalon. *J. Comp. Neurol.* **506**, 16-29. doi:10.1002/cne.21529

Yu, G., Wang, L.-G., Han, Y. and He, Q.-Y. (2012). clusterProfiler: an R package for comparing biological themes among gene clusters. *OMICS* **16**, 284-287. doi:10.1089/omi.2011.0118

Zhang, Y., Liu, T., Meyer, C. A., Eeckhoute, J., Johnson, D. S., Bernstein, B. E., Nusbaum, C., Myers, R. M., Brown, M., Li, W. et al. (2008). Model-based analysis of ChIP-Seq (MACS). *Genome Biol.* **9**, R137. doi:10.1186/gb-2008-9-9-r137

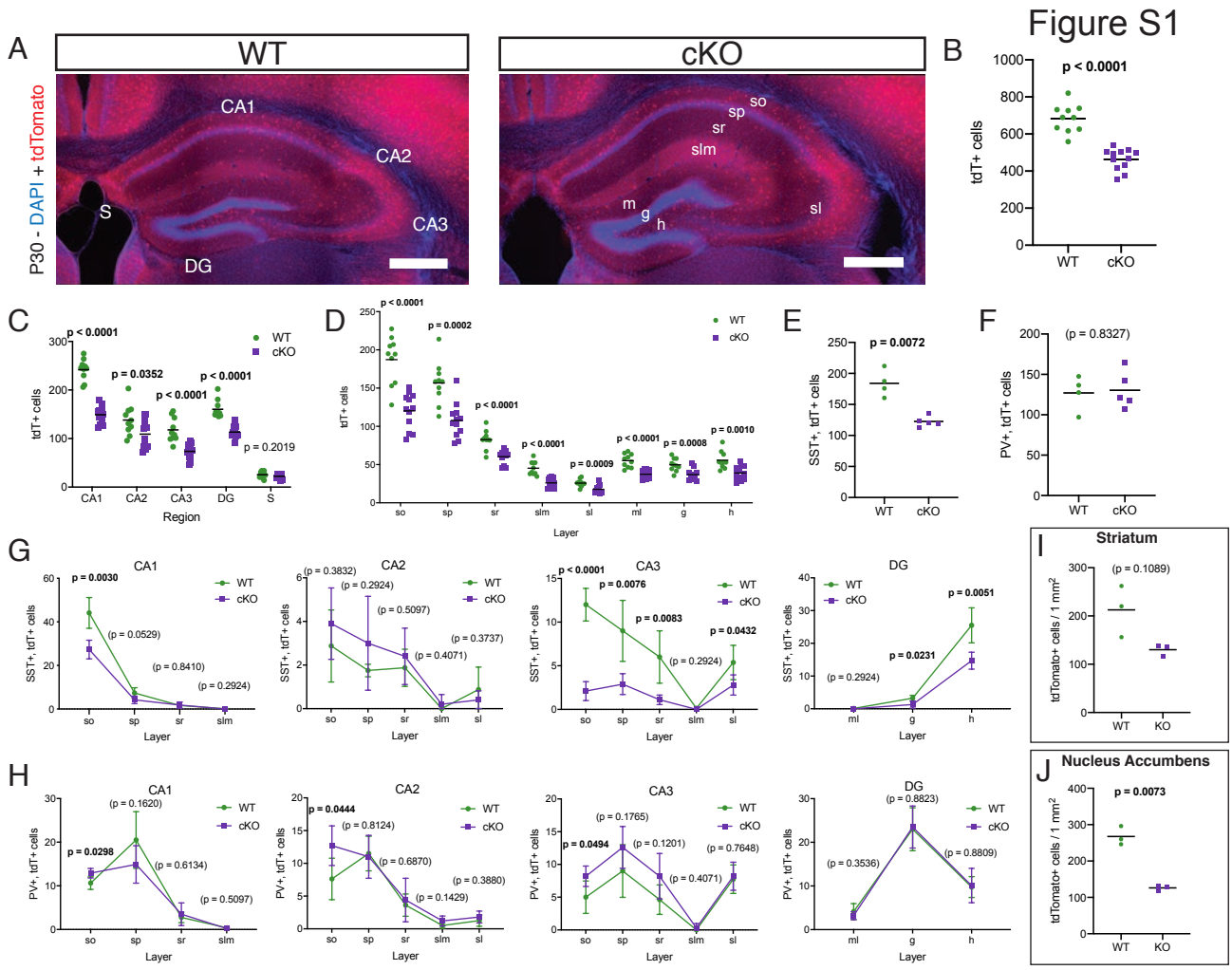

Figure S1, related to Figure 1. Deletion of *Prdm16* in the *Nkx2.1* lineage causes loss of hippocampal interneurons. A) Representative images of the hippocampus of WT and cKO mice at P30, after immunofluorescence staining for tdTomato (red), counterstained with DAPI (blue). Scale bars, 500 *μ*m. Area labels (WT image): CA – *cornus Ammonis* (Ammon's horn) regions 1, 2 and 3; DG – dentate gyrus; S – subiculum. Layer labels (cKO image): so – *stratum oriens*; sp – *stratum pyramidale*; sr – *stratum radiatum*; slm – *stratum lacunosum moleculare*; sl – *stratum lucidum*; ml – molecular layer; g – granule cell layer; h – hilus. **B)** Quantification of the number of tdTomato+ cells in the entire hippocampus of WT (green squares) and cKO (purple circles) mice (n = 10 for WT, n = 12 for cKO). **C)** Quantification of the total number of tdTomato+ cells across different areas of the entire hippocampus in WT and cKO mice at P30.

D) Quantification of the number of tdTomato+ cells across different cellular layers in the entire hippocampus of WT and cKO mice at P30. **E)** Quantification of the total number of somatostatin+ cells in the entire hippocampus of P30 WT (n = 4) and cKO (n = 5) mice. **F)** Quantification of the total number of somatostatin+ cells in the entire hippocampus of P30 WT (n = 4) and cKO (n = 5) mice. **G, H)** Analysis of the distribution of tdTomato+ cells costained for SST (**G**) or PV (**H**) across the indicated layers of the hippocampus of P30 WT and cKO mice in areas CA1, CA2, CA3 and DG. **I, J)** Quantification of the number of tdTomato+ cells in the striatum (**I**) and nucleus accumbens (**J**) of P30 WT and cKO mice (n=3 mice per genotype). Means ± S.D. are represented. Unpaired t-tests with Welch's correction (panels **B**, **E**, **F**) or multiple t-tests (panels **C**, **D**) were performed; p-values are indicated above the corresponding compared sets of data: those highlighted in bold represent significant differences ($p<0.05$).

Figure S2

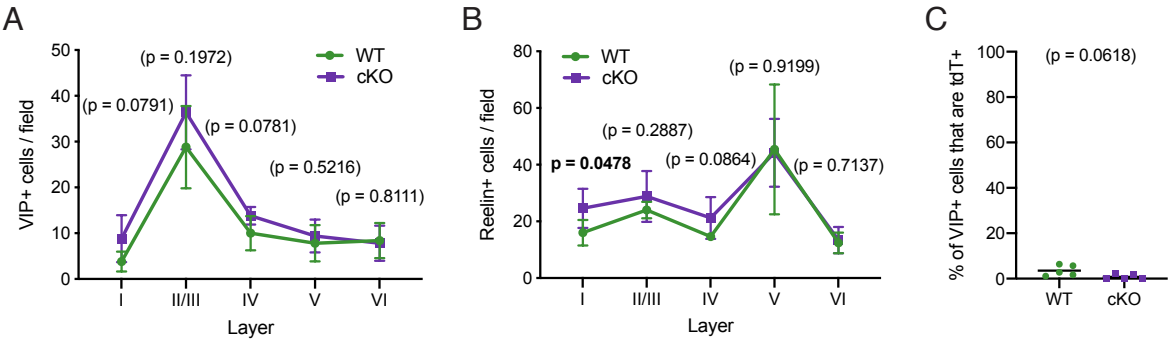

Figure S2, related to Figure 2. Partial compensation of depleted MGE-derived interneurons is restricted to the reelin+ population in upper layers. A) Number of VIP+ cells in each indicated cortical layer, per 1 mm-wide column. **B)** Number of reelin+ cells in each indicated cortical layer, per 1 mm-wide column. **C)** Percentage of VIP+ cells costained for tdTomato. Multiple t-tests (panels **A** and **B**) or unpaired t-tests with Welch's correction (panel **C**) were performed; p-values are indicated above the corresponding compared sets of data: those highlighted in bold represent significant differences ($p<0.05$).

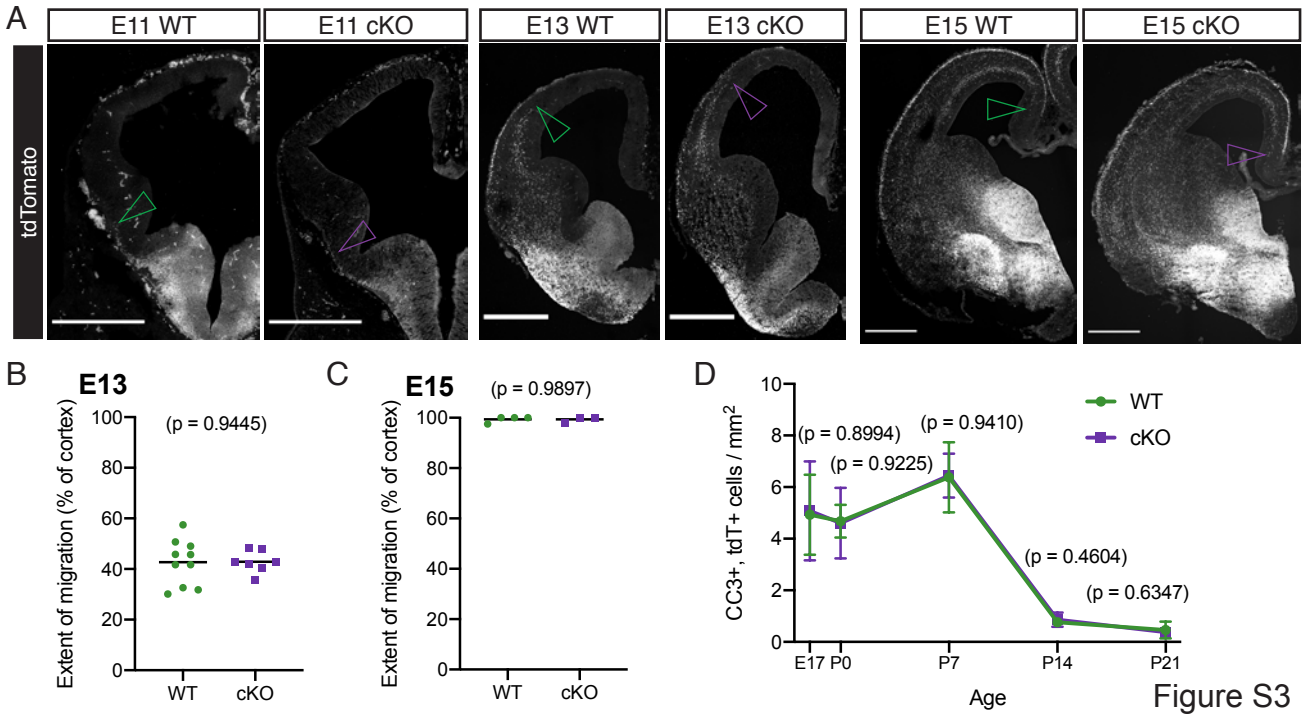

Figure S3

Figure S3, related to Figure 4. Loss of cortical interneurons is not due to defects in migration or increased cell death. A) Overview of the migration of Nkx2.1-lineage cells (expressing tdTomato, white) within coronal hemisections of WT and cKO brains at E11, E13 and E15. Empty arrowheads indicate the extent of migration of MGE-derived interneurons into the cortex within each section. Scale bars, 500 μm. **B, C)** Quantification of the extent of migration of Nkx2.1-lineage cells into the cortex, expressed as % of the length of the cortex occupied by tdTomato+ cells in WT (green circles) and cKO (purple squares) embryos at E13 (**B**) and E15 (**C**). **D)** Quantification of the number of cells costained with tdTomato (tdT+) and the apoptotic marker cleaved caspase 3 (CC3+) per mm^2 in the cortex of WT (green circles) and cKO (purple squares) mice at the indicated developmental stages. Error bars represent S.D. Unpaired t-tests with Welch's correction (panels **B** and **C**) or multiple t-tests (panel **D**) were performed; p-values are indicated above the corresponding compared sets of data.

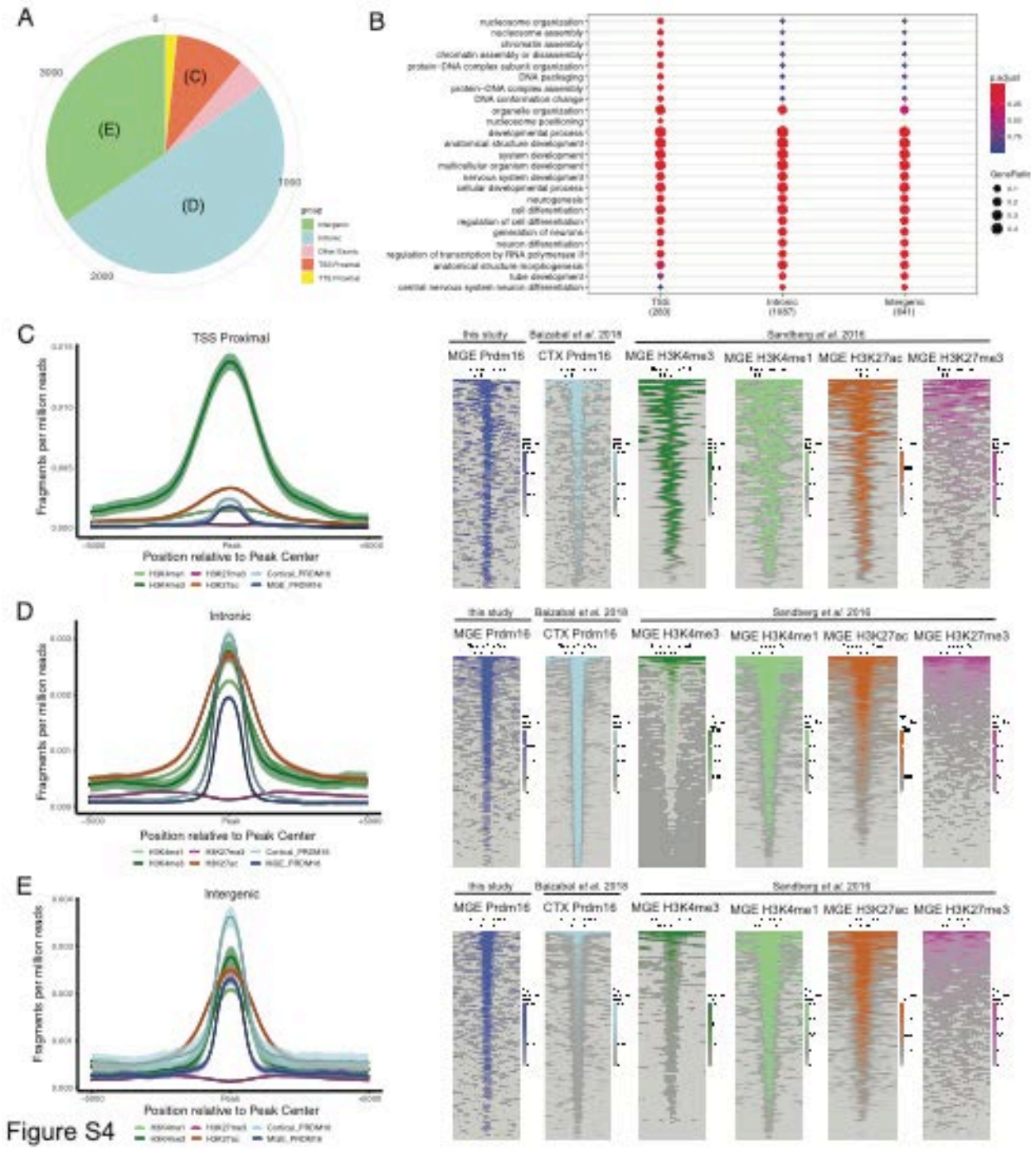

Figure S4

Figure S4, related to Figure 6. Comparison of PRDM16 ChIP-Seq peaks between cortex and MGE. A) Genome-wide distribution of E15 cortex PRDM16 ChIP-Seq peaks relative to gene annotations (TSS: transcription start site; TTS: transcription termination site). **B)** Top 30

gene ontology term enrichment in genes closest to PRDM16 ChIP-Seq peaks from E14 MGE (this study) and E15 cortex (Baizabal et al., 2018) experiments. Categories represent all PRDM16 peaks from both sets of experiments ('All'), common to both datasets ('Both'), or exclusive to either the cortex ('Cortical Only') or the MGE ('MGE Only'). **C-E)** Read density in several embryonic ChIP-Seq experiments (aggregate line plots are shown on the left, and heatmaps are shown on the right). The peaks were grouped and analyzed by the location in either TSS (**C**), intronic (**D**) or intergenic (**E**) genomic regions. Data were generated for this study from E14 MGE (dark blue), or obtained from (Baizabal et al., 2018) (CTX, ChIP-Seq for PRDM16 in E15 cortex; light blue) and (Sandberg et al., 2016) (ChIP-Seq for each specified histone modification in E13 MGE; all other plots).

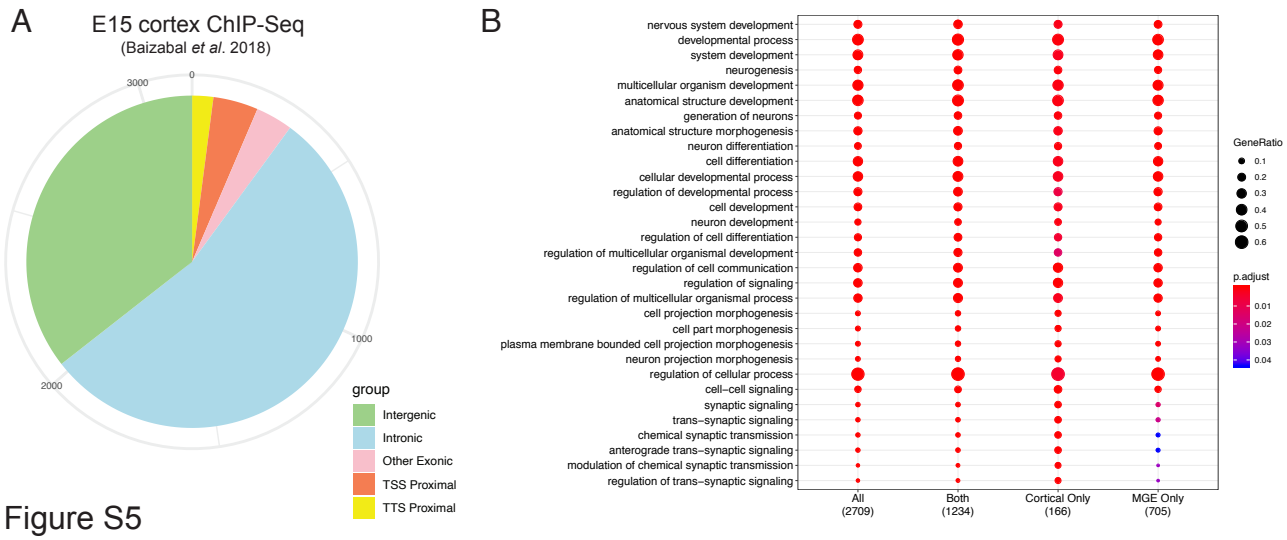

Figure S5

Figure S5, related to Figure 6. Analysis of PRDM16 peaks relative to their genomic location. A) Genome-wide distribution of E13 MGE PRDM16 ChIP-Seq peaks relative to gene annotations (TSS: transcription start site; TTS: transcription termination site) – note: this panel is the same data displayed as **Figure 6C**, and is included here just for clarity. **B)** Top 30 gene ontology term enrichment in genes closest to PRDM16 ChIP-Seq peaks located in TSS, intronic or intergenic locations, as indicated.

Table S1. Differentially regulated genes (RNA-Seq)

Click here to Download Table S1

Table S2. All PRDM16 MGE peaks

Click here to Download Table S2

Table S3. All PRDM16 peaks

Click here to Download Table S3

Table S4. PRDM16 peaks common to cortex and MGE

Click here to Download Table S4

Table S5. PRDM16 peaks exclusive to MGE

Click here to Download Table S5

Table S6. PRDM16 peaks exclusive to cortex

Click here to Download Table S6

Table S7. Overlapping PRDM16/ASCL1 peaks

Click here to Download Table S7

Table S8. Gene list comparisons

Click here to Download Table S8

Table S9. Reagents and resources

REAGENT or RESOURCE	SOURCE	IDENTIFIER
Antibodies		
Chicken polyclonal anti-GFP	Aves	Cat # GFP-1020
Rat monoclonal anti-pH3	Abcam	Cat # ab10543
Guinea pig polyclonal anti-PRDM3/PRDM16	Jeremy Dasen, NYU	N/A
Rabbit polyclonal anti-PRDM16	Patrick Seale, UPenn	N/A
Mouse monoclonal anti-Parvalbumin	Sigma	Cat # SAB4200545
Mouse monoclonal anti-Reelin	Millipore	Cat # MAB5364
Chicken polyclonal anti-RFP	Rockland	Cat # 600-901-379
Rabbit polyclonal anti-Somatostatin	Peninsula	Cat # T-4103
Rabbit polyclonal anti-VIP	Immunostar	Cat # 20077
Goat polyclonal anti-chicken Alexa 488	Thermo Fisher	Cat #A11039
Goat polyclonal anti-chicken Alexa 546	Thermo Fisher	Cat #A11040
Goat polyclonal anti-guinea pig Alexa 488	Thermo Fisher	Cat #A11073
Goat polyclonal anti-mouse Alexa 488	Thermo Fisher	Cat #A11001
Goat polyclonal anti-mouse Alexa 647	Thermo Fisher	Cat #A21236
Goat polyclonal anti-rabbit Alexa 488	Thermo Fisher	Cat #A11034
Goat polyclonal anti-rabbit Alexa 647	Thermo Fisher	Cat #A21245
Goat polyclonal anti-rat Alexa 488	Thermo Fisher	Cat #A11006
Bacterial and Virus Strains		
Replication-incompetent eGFP-expressing retrovirus	(Palmer et al., 1999)	N/A
Critical Commercial Assays		
RNAscope V2 Reagent Kit	Advanced Cell Diagnostics	Cat # 323100
Deposited Data		
Experimental Models: Cell lines		
HEK293 retrovirus packaging cell line	(Palmer et al., 1999)	293 gp NIT-GFP
Experimental Models: Organisms/Strains		
Mouse: CD-1	Charles River	Strain code 022
Mouse: C57BL/6J-Tg(Nkx2-1-cre)2Sand/J (Nkx2.1-Cre)	Jackson Laboratory	Stock no. 008661
Mouse: B6.129-*Prdm16*$^{tm1.1Brsp}$/J (Prdm16$^{f/f}$)	Jackson Laboratory	Stock no. 024992
Mouse: B6.Cg-*Gt(ROSA)26Sor*$^{tm14(CAG-tdTomato)Hze}$/J (Ai14)	Jackson Laboratory	Stock no. 007914
RNAscope probes		
Lmo1	Advanced Cell Diagnostics	Cat # 511211-C3
Pdzrn3	Advanced Cell Diagnostics	Cat # 517061
tdTomato	Advanced Cell Diagnostics	Cat # 317041
Software and Algorithms		
ImageJ 1.52o	(Schneider et al., 2012)	http://imagej.nih.gov/ij
Fiji 2.0.0-rc-68/1.52g	(Schindelin et al., 2012)	http://fiji.sc
Prism 7, Prism 8	GraphPad	
MATLAB	Mathworks	
Igor Pro	Wavemetrics	